

# Hierarchical, Porous Hydrogels Demonstrating Structurally Dependent Mechanical Properties

**Elisabeth Lloyd**

Pennsylvania State University

**Rami Alhasan**

Brigham Young University <https://orcid.org/0000-0002-8215-3793>

**Sujata Dhakal**

Case Western Reserve University

**Svetlana Morozova**

Case Western Reserve University

**Douglas Tree**

Brigham Young University

**Robert Hickey**

[r.jh64@psu.edu](mailto:r.jh64@psu.edu)

Pennsylvania State University <https://orcid.org/0000-0001-6808-7411>

---

## Article

### Keywords:

**Posted Date:** May 30th, 2023

**DOI:** <https://doi.org/10.21203/rs.3.rs-2954017/v1>

**License:**   This work is licensed under a Creative Commons Attribution 4.0 International License.

[Read Full License](#)

**Additional Declarations:** There is **NO** Competing Interest.

---

# Abstract

While hierarchical ordering is a distinctive feature of natural tissues and is directly responsible for their diverse and unique properties, research efforts to synthesize biomaterials have primarily focused on using molecular-based approaches without considering multiscale structure. Here, we report a bottom-up self-assembly process to produce highly porous hydrogels that resemble natural tissues both structurally and mechanically. Randomly oriented, physically crosslinked nanostructured micelles form the walls of aligned, polymer-rich pore walls that surround water-rich cavities. Extremely soft elastic modulus ( $< 1$  kPa), highly stretchability (greater than 12-times), strain-hardening, and completely reversible deformation result from the hierarchical structure. Independent control of nano and macroscales is realized through the combination of polymer macromolecular parameters and processing conditions, directly impacting the resulting phase behavior. Here, we demonstrate precise control of the material structure and structure orientation over many orders of magnitude (e.g., nm –  $\mu$ m), and reveal how the multiscale structure directly impacts mechanical properties.

## Main

Biological tissues exhibit complex and hierarchically ordered structures while producing a diverse range of properties from a limited number of components.<sup>1-3</sup> Several key properties are critical to replicate natural tissues: biomimetic strain-hardening,<sup>4</sup> highly reversible deformation,<sup>5,6</sup> and a microstructure conducive to cell proliferation.<sup>7</sup> Hydrogels are desirable materials for mimicking natural tissues due to their high water content<sup>8-10</sup> – enabling transport of nutrients and waste products to and from cells – but crosslinked hydrogels composed of a single polymer network exhibit a limited range of mechanical properties.<sup>11,12</sup> Advances in synthetic chemistry have broadened this range,<sup>13-16</sup> but these hydrogels approach mimicking natural tissues from a molecular standpoint, and frequently lack any degree of ordering beyond their molecular networks. Introducing porous microstructures in hydrogels to control multiscale structures typically leads to brittle materials.<sup>17</sup> Therefore, new methods combining synthetic advances with self-assembly are necessary to control hierarchical structure and property.

Recently, we demonstrated a rapid injection processing method to produce highly extendable, reversibly deformable, and extremely soft hierarchical hydrogels.<sup>18</sup> Additionally, the exceptional mechanical properties afford the hydrogels the ability to be processed into nanostructured polymer muscles demonstrating linear and rotary actuation.<sup>19</sup> When an amphiphilic ABA triblock copolymer containing hydrophobic and hydrophilic A and B domains, respectively, is dissolved in a water-miscible organic solvent and injected into water, the block copolymer will self-assemble at both the nano and macroscales (Fig. 1a).<sup>18,20</sup> The hydrophobic end-blocks self-assemble into micelle cores bridged by the hydrophilic mid-blocks, forming the network.<sup>18,20</sup> In addition to nanoscale self-assembly, macroscale pores form within this network due to solvent exchange with the water bath, resulting in a physically crosslinked nanoscale micelle network encapsulating micrometer sized water pores (Fig. 1b) that are reminiscent of the extracellular matrix of skeletal muscles (Fig. 1c).<sup>21</sup> Hydrogels possessing this unique hierarchical

structure exhibit drastically different mechanical properties than traditional physically crosslinked hydrogels prepared from the same ABA triblock copolymers,<sup>22</sup> yet a fundamental understanding of multiscale structure formation during processing and the impact of morphology on mechanical properties is still an open question.

Here, we reveal design rules to independently control both nano and microscale ordering – and thus mechanical properties – of the hierarchical hydrogels. Tunable porous microstructures are realized by varying the concentration of a single poly(styrene)-block-poly(ethylene oxide)-block-poly(styrene) (SOS) triblock copolymer and the organic solvent used in the initial solution. An additional level of hierarchy forms in hydrogel fibers made from *N,N*-dimethylformamide (DMF), where the hydrogels exhibit a coaxial or core-sheath morphology. In contrast, hydrogel fibers made with tetrahydrofuran (THF) show a monomodal pore distribution. Interestingly, there is essentially no variation in the randomly oriented nanoscale ordering of the micelles with respect to processing conditions, which is attributed to the SOS molecular weight and block volume fraction.<sup>23</sup> The coaxial fibers made using DMF show a strong strain-hardening response at high strain that is reminiscent of natural tissues.<sup>4</sup> Simultaneously controlling multiscale structure and orientation over drastically different length scales using a single processing step, to the best of our knowledge, has yet to be demonstrated in any material system, and is critically important in creating next generation biomaterials.

## Preparing hierarchical hydrogels

Hierarchical hydrogels were produced using a SOS polymer with a number-average molecular weight ( $M_n$ ), an O-block volume fraction ( $f_0$ ), and a dispersity ( $\mathcal{D}$ ) of 192 kg/mol, 0.9, and 1.05, respectively. An O-block volume fraction of 0.9 was targeted to promote the formation of a disordered spherical micelle morphology at the nanoscale and to increase the extensibility of the hydrogels.<sup>18</sup> Additionally, the S-end blocks were selected as the hydrophobic moiety in the triblock copolymer due to the high glass transition temperature ( $T_g$ ), preventing chain pull-out and improving mechanical stability.<sup>18</sup>

Two different water-miscible organic solvents were examined, THF and DMF, to explore the impact of processing conditions hydrogel structure. The polarity of the water-miscible organic solvent is known to impact the nanoscale solution-phase self-assembly of amphiphilic block copolymers,<sup>24,25</sup> yet the effect on micrometer length scale organization is unknown. The physically crosslinked spherical micelle network that forms at the nanoscale is primarily dictated by the molecular weight and  $f_0$  of the block copolymer. Previous studies have found that the initial polymer solution must be at or above the entanglement concentration to form hydrogels, and thus, all hydrogels were prepared using initial solution concentrations between 8–15 wt%. The concentration range allows for the hydrogel structure to be investigated at either constant polymer solution concentration or viscosity to isolate the effects of varying the organic solvent (**Figure S2**). The water swelling ratios of the prepared hydrogel fibers were unusually high –  $\approx 98\%$  water by weight – and remarkably consistent across sample conditions (**Figure S3**). The consistency in water content is particularly noteworthy, as physically crosslinked triblock

copolymer hydrogels prepared using traditional preparation methods (e.g., thermally annealing the neat SOS polymer and then hydrating) are typically 4–40% water by weight.<sup>22</sup>

## Micelle nanostructure

The nanoscale structure of the hydrogels was characterized using transmission electron microscopy (TEM) and small-angle X-ray scattering (SAXS). Micelles were visualized by characterizing physically crosslinked micellar aggregates, or “microgels”, formed by injecting a polymer solution with a reduced polymer concentration into water.<sup>18</sup> The microgels are dispersible in the aqueous solution and easily drop-cast onto a TEM grid and dried. The micelle diameter resulting from the use of either solvent was measured to be  $20 \pm 1$  nm (Fig. 2a). While the diameter of spherical micelles is known to depend on polymer concentration and solvent,<sup>23</sup> the relatively narrow 8–15 wt% concentration range and large O-block volume fraction resulted in a consistent micelle size.<sup>23</sup>

Synchrotron SAXS measurements were used to investigate the organization of the spherical micelles in the hydrogel fibers. The one-dimensional (1D) scattering intensity versus scattering vector ( $q$ ) shown in Fig. 2b indicates that the primary scattering peak ( $q^*$ ) for all samples is located at  $q \approx 0.007 \text{ \AA}^{-1}$ , regardless of the organic solvent or polymer solution concentration. Moreover, the 2D SAXS plots indicate that the micelles are randomly oriented. The 1D scattering plots were further analyzed by fitting them to a spherical form factor and Percus-Yevick hard sphere approximation structure factor (Fig. 2c) (See Supporting Information).<sup>26</sup> Three fitting parameters were used for the model: 1) micelle diameter, 2) micelle center-to-center distance (i.e., domain spacing), and 3) the micelle volume fraction (Fig. 2c, **insert**).

The measured domain spacing and micelle diameter from SAXS is highly consistent for all processing conditions at approximately  $84 \pm 3$  nm (Fig. 2d, e), and the micelle diameter values calculated from SAXS agree with the micelle diameter measured from TEM. The high degree of reliability in the domain spacing, despite variations in the viscosity and solvent, indicates the nanostructure is insensitive to shear at the injection rates used in the study. The nanostructure in the absence of shear was characterized by adding the initial polymer solution into a mold and submerging in a water bath. Even under these circumstances, the micelle size remained unchanged, confirming that – for the SOS used here – the micelle nanostructure is unaffected by processing parameters when using rapid injection processing.

Physical hydrogels only possessing nanoscale ordering were produced from the block copolymer produced using conventional annealing methods to compare to the hierarchical hydrogels.<sup>22</sup> The SAXS plots in Fig. 2f show the clear disordered sphere morphology of the dry annealed SOS sample, with a reduced domain spacing compared to the hydrogel fibers. The primary scattering peak associated with the micelle center-to-center distance shifts to lower  $q$  on hydration, indicating an increase in the domain spacing due to the swelling of the polymer (Fig. 2f). The conventional hydrogel exhibits a reduced degree of water swelling (15 wt% versus 98% for hierarchical hydrogels) yet possesses a much larger domain spacing of 97 nm, relative to  $84 \pm 3$  nm for the hierarchical hydrogels. The difference in micelle center-to-

center distances between the hydrogels is attributed to the pore walls in the hierarchical structure, in which the micelles are more closely packed.

## Porous microstructure

The porous microstructure of the hierarchical hydrogels was characterized using cryogenic scanning electron microscopy (cryo-SEM) (Fig. 3). Hydrogel samples for cryo-SEM were prepared by first vitrifying the hydrated sample in liquid nitrogen and then cryo-milling perpendicular to the fiber length to produce a clean cross-section (see Supporting Information). Though some samples contained ice within the pores that did not sublime fully under vacuum, the pore walls are still clearly visible.

The initial water-miscible organic solvent plays a drastic role in the microscale structure that forms (Fig. 3). Samples produced using DMF exhibit a coaxial morphology (Figs. 3a-c), where the outer edge of each fiber is comprised of large pores, while the inner core contains exclusively small pores. The demarcation between regions is sharp and distinct, and the outer region depth averages 200–240  $\mu\text{m}$ . Remarkably, the outer and inner pore sizes are consistent across all DMF concentrations, approximately 30  $\mu\text{m}$  and 5  $\mu\text{m}$ , respectively (Fig. 3h).

In contrast, hydrogels prepared using THF exhibit a monomodal pore distribution (Figs. 3d - f), where the average pore size – weighted according to the relative fraction of cross-sectional area composed of large outlier pores – decreases from  $30 \pm 13 \mu\text{m}$  to  $9 \pm 4 \mu\text{m}$  as concentration increases from 11 wt% to 14.5 wt%, respectively (Fig. 3h). Furthermore, the pores size distribution in hydrogels prepared using THF narrows with increasing concentration as the pores become more regular in shape. At high concentrations, the pores resemble those found in the inner small-pore region of the samples prepared using DMF (Fig. 3g), though slightly larger in size (Fig. 3h). Small-angle light scattering (SALS) measurements for a hydrogel prepared at a 12.5 wt% polymer solution in THF reveal that the micrometer pores are cylindrical in geometry and are aligned along the fiber direction (Fig. 3i).<sup>27</sup> The SALS results confirm that the micrometer pores form during solvent exchange and not an artifact of vitrification.

## Factors dictating the self-assembly of the porous microstructure

The microstructure of the hydrogels is expected to form when the system enters the spinodal region of the polymer/solvent/water ternary phase diagram during solvent exchange. Although nonsolvent-induced phase separation (NIPS), used to create asymmetric membranes, utilizes spinodal decomposition to control structure, the established parameters shown to dictate the microstructure in NIPS systems – polymer solution viscosity and solvent exchange<sup>28</sup> – do not translate for the reported hydrogel system. Both solution viscosities and solvent diffusion coefficients are nearly identical between THF and DMF samples, and therefore cannot explain the difference in microstructure (see Supporting Information). Thus, we hypothesize the microstructural differences are the result of spinodal decomposition pathways that vary between solutions. To this end, a modified random phase approximation (RPA) was used to

predict the ternary phase diagram for hydrogels prepared using DMF and THF.<sup>29</sup> Furthermore, by incorporating the measured solvent exchanged rates into the phase diagram, it is possible to predict the point the system enters the two-phase region of the ternary phase diagram.

A parameterized RPA model of an ABA triblock copolymer solution was used to compute spinodal curves within the ternary phase diagrams for the two relevant systems: SOS/THF/water and SOS/DMF/water (Figs. 4a - c).<sup>30-32</sup> The full diagrams of the systems (an example of which is shown in Fig. 4a) show regions of micro- and macrophase separation, with the macrophase region residing at increased water content. Figures 4b and 4c show the area of interest at the top of the phase diagrams, with the initial compositional changes for each sample plotted up until the samples are fully within the macrophase-separated region. There is a subtle but important difference in the macrophase segregation ( $2\phi$ ) region between the diagrams: DMF solutions are more stable at low water concentration than in THF, which is indicated by a “turning over” of the two-phase region in Fig. 4c relative to Fig. 4b. The difference in phase diagrams is due to the compatibility between DMF/THF and the O-block in SOS (see **Table 2** in the Methods Section).

The difference in phase behavior is not sufficient by itself to explain hydrogel microstructure. According to NIPS theory,<sup>33,34</sup> microstructure is determined by the trajectory the system takes in concentration space as water is exchanged for solvent in the hydrogel. The trajectory was computed using a two-phase/1D diffusion model of the ternary system as described in the Methods section below. Figure 4d shows a simulation snapshot after significant solvent/water exchange for a hydrogel fiber that is initially 11 wt% polymer ( $\phi_{\text{SOS}}$ ) and 89 wt% THF ( $\phi_{\text{THF}}$ ). The snapshot shows a hydrogel fiber phase (right) that is swelling as water diffuses in and THF diffuses to the bath (left). Averaging the concentration over the fiber thickness and plotting the concentration in time gives trajectories (green line) for THF/water exchange and DMF/water exchange in Figs. 4b, 4c, respectively.

The solvent/water exchange trajectories combined with the ternary phase diagrams provide a plausible hypothesis for the difference in hydrogel microstructure. Figure 4b shows that a THF/water exchange trajectory with an initial SOS concentration of 11 wt% (the darkest green) almost immediately enters the two-phase region, experiencing a near-immediate macrophase separation. By contrast, Fig. 4c shows that a DMF/water trajectory with an initial SOS concentration of 11.5 wt% (the lightest green) experiences a significant lag before it macrophase separates. We conjecture that a delay before phase separation leads to the existence of a concentration gradient across the fiber. We note that the model does not predict a coaxial morphology with a sharp distinction between pore sizes or the impact of the metastable region located in between the spinodal and binodal phase boundaries on the microstructure. Thus, a more detailed model is needed to capture these phenomena.

## Microstructure dependent mechanical properties

Uniaxial extension measurements performed on the hydrogel fibers demonstrate that the microstructure plays a critical role in the mechanical properties (Figs. 5a, b). Despite the low elastic modulus of the hydrogel fibers (e.g., < 1 kPa) all samples reversibly stretch to many times their initial length, which, to our knowledge, has never been reported in highly porous hydrogels (see Supporting Video 1). Samples produced with DMF possess near-identical microstructures and have highly consistent deformation responses, while the samples produced using THF show a steady increase in the ultimate tensile strength of the hydrogels as the average pore size decreases, which is in agreement with previously published work.<sup>18</sup> The Young's modulus,  $E$ , and toughness of the hydrogels follow a similar trend (Fig. 5b), which is inversely correlated with average pore size (Fig. 3h). Hydrogel samples produced using DMF display both strain-hardening behavior and a significant increase in elongation at break, which might be attributed to their coaxial morphologies. Furthermore, all hydrogel fibers reversibly extend for at least five loading and unloading cycles with no hysteresis (Fig. 5c).<sup>35</sup> Reversible deformation and strain hardening, two hallmark traits of natural tissues, are highly difficult to mimic in hydrogel materials, and are the result of the hierarchical ordering present in the fibers.

The introduction of aligned pores into the micelle network produces an additional deformation mechanism, where pores initially deform at low strain, then stress is gradually transferred to the O-blocks bridging the PS micelle cores (Fig. 5e). Both these deformation mechanisms are fully elastic, leading to the full recovery of mechanical properties after stretching. The proposed multi-deformation mechanism is supported via *in situ* SAXS measurements, where the micelle center-to-center distance is constant (i.e., minimal change in the  $q$ -value) up to an elongation ratio of five when uniaxially extended (Fig. 5d). Higher elongation ratios could not be investigated because the signal significantly decreased with extension due to the reduced cross-sectional area. Furthermore, pore deformation observed via *in situ* SALS shows an increase in pore orientation and a decrease in domain spacing at low to moderate strain (Fig. 5e, **Figure S27**), which demonstrates that the pores are deforming while the micelle spacing remains constant.

These materials exhibit multiple levels of hierarchical ordering, resulting in extremely low moduli and tensile strength, extremely high extensibility, minimal hysteresis, and strain-hardening behavior. While one or more of these properties can be produced in synthetic hydrogels, the combination of these properties in a porous hydrogel is unprecedented. Physical hydrogels without the hierarchical ordering demonstrated here exhibit a narrow range of properties<sup>22,36,37</sup>, and porous gels previously reported are historically quite brittle (Fig. 5f).<sup>17, 38-43</sup> The flexibility of the hierarchical hydrogels is rivaled only by supramolecular<sup>39,44,45</sup> and interpenetrating network hydrogels,<sup>46-49</sup> but these materials frequently suffer from limited reversibility due to non-elastic deformation mechanisms. Self-assembling bottlebrush elastomer hydrogels demonstrate strain-hardening responses similar to natural tissue,<sup>4,50</sup> but these materials lack the porous structure or hierarchical ordering that is critical for synthetic biomaterials. While future investigation is needed to determine the precise impact of molecular architecture and expand the accessible mechanical property range via altering the block copolymer compositions, these hydrogels represent an exciting new class of hydrogels for biomaterial applications.

# Outlook

Here, we demonstrate a facile method to produce hierarchical porous hydrogels, driven by the self-assembly of hydrophobic domains and rapid solvent exchange when the polymer solution is injected into a water bath. Unlike many synthetic biomaterial approaches, which focus on replicating the properties of tissues in bulk materials, this research reveals hierarchically ordered, self-assembling hydrogels with properties dependent on the microstructure. The highly aligned porous structure of these hydrogels enables completely reversible elastic deformation at strains easily up to six times the initial length. While the reported hydrogels are significantly more elastic than many natural tissues, the system possesses many avenues for modification of the microstructure and thus mechanical properties. RPA theory and a 1D transport models will aid in building design rules to rationally explain and target future materials with desired properties. Despite the wide variety in microstructure and mechanical properties, these hydrogels exhibit no change in the micelle nanostructure and water swelling ratio, allowing the microstructure to be tuned independently from the nanostructure. The reported hydrogels and rapid injection processing will potentially lead to a new class of customizable cell scaffolds and biomedical materials, with a diverse range of mechanical properties that are finely tuned through the selection of the initial amphiphilic block copolymer architecture and subsequent processing parameters.

## Methods

### Amphiphilic triblock copolymer synthesis

Poly(styrene)-poly(ethylene oxide)-poly(styrene) (SOS) triblock copolymers were chosen as a representative amphiphilic triblock copolymer for this system due to the enhanced mechanical properties due to the high glass transition of poly(styrene), which aids in stabilizing the micelle structure.<sup>18</sup> The triblock copolymer used in this research was synthesized via sequential living anionic polymerization, which has been previously described.<sup>18</sup> After each step in the synthesis process, the molecular weight and dispersity were determined using size-exclusion chromatography, while the volume fraction of the polymers in the material were characterized via proton nuclear magnetic resonance spectroscopy. The supporting information contains more detailed synthetic information and characterization results.

### Characterization of the block copolymer solutions

Two solvents were used as water-miscible organic solvents for the precursor solutions: tetrahydrofuran (THF, Sigma Aldrich,  $\geq 99.9\%$ ) and dimethylformamide (DMF, Sigma Aldrich anhydrous 99%). The critical water concentrations for micellization for the polymer in different solvents were determined by light scattering experiments of dilute amphiphilic block copolymer solutions in organic solvent with increasing addition of water, similar to previous reported studies.<sup>19</sup> The viscosity of the polymer solutions at high concentrations and solvents was determined using a Discovery Hybrid Rheometer at room temperature with parallel plate geometry. A solvent trap was used to prevent the evaporation of the more volatile THF

solvent. The trends calculated from this data were used to match the viscosities of the solutions between the solvents.

## Hydrogel processing

**Rapid Injection Processing:** Polymer solutions were injected into coagulation bath containing RO water using a syringe pump set to an injection speed of 1 mL/min and a needle gauge of 19. Initial solutions were used with concentrations ranging from 8–15 wt%. Though the gel fibers formed almost instantly on contact with water, they were left in the water bath for an hour to ensure complete solvent diffusion, then transferred to vials of RO water for storage at 4°C.

**Conventional Hydrogels:** Conventional physically crosslinked triblock copolymer hydrogels were produced by thermally annealing the neat SOS polymer above the O-block and S-block crystallization and glass transition temperature, respectively, and then swelling with water. Specifically, hydrogels were prepared by first annealing the triblock copolymer in a thermal press at 100 psi and 150°C for 30 min, followed by annealing under vacuum for 24 h at 150°C. After cooling, the annealed sample was hydrated in pure RO water for 3 d to ensure total hydration.

## Nanoscale characterization

The micellar nanostructure was characterized using a synchrotron X-ray source at the National Source for Light Scattering II at Brookhaven National Laboratory, both under static conditions, and *in situ* under extension using a Linkham tensile stage. The data was fitted using the IRENA scattering package for Igor 9 Pro using the Percus-Yevick approximation for hard spheres to calculate micelle core diameter, center-to-center distance, and micelle volume fraction. Microgels formed from a semi-dilute solution of the triblock copolymer injected into water were drop cast onto a TEM grid could be used to approximate the micelle diameter. The microgel samples were stained with a 2 wt% solution of uranyl acetate in water and imaged using an FEI Tecnai BioTwin TEM.

## Microstructure characterization

Hierarchical hydrogel microstructure was characterized using cryogenic scanning electron microscopy (Cryo-SEM). Hydrogel cross-sections were prepared by mounting the sample on aluminum pins, vitrified in liquid nitrogen, and cryo-milled to reveal the hydrogel cross-section. Hydrogels were stored under liquid nitrogen, then transferred to a Zeiss Cryo-SEM for imaging at -125°C. Water was partially sublimated at -95°C, then the sample was sputter coated with a gold-palladium alloy. Pore sizes were measured using Image J. An example of pore size measurement is shown in the Supporting Information.

The inter pore spacing and alignment was characterized via small-angle light scattering (SALS). An incident laser of 625 nm was scattered from the samples at an angle  $\theta$  through a convex lens L1 (Edmund Optics-NT67-245) with a numerical aperture, N.A. = 0.85 that captures up to 58° scattered light.<sup>27</sup> The converging scattered light then passes through beam stop and is refocused through another convex lens L2 (Thorlabs-LA 1951A). The beam stop is at a focal length away from lens L1 and blocks all

direct light from the laser. The  $l_1$  and  $l_2$  can be changed to optimize the  $q$ -range.<sup>27</sup> The scattered light is then projected onto a CMOS detector, D (Basler acA800-510 um) which is a focal length away from L2.<sup>27</sup>

## Uniaxial extension measurements

The mechanical properties of the hydrogels were characterized via uniaxial extension using an MTS Criterion load frame equipped with a 10 N force transducer. The hydrogels were secured with spring-action tensile grips to minimize hydrogel slip during extension and strained at a rate of 3/min. To determine the cross-sectional area, hydrogel cross-sections were placed on a glass slide and imaged using an Olympus optical microscope. Hysteresis was determined by repeatedly straining the hydrogel to five times its original length for five cycles.

## Rheological characterization

The viscosity of polymer solutions at various polymer concentrations was measured using a Discovery HR-3 Hybrid Rheometer at room temperature, equipped with a solvent trap to prevent evaporation, which is critical for THF samples at high polymer concentrations. Solutions in the entangled regime were measured with a 2 cm parallel plate geometry, while semi-dilute solutions used a 6cm parallel plate geometry. The solutions were tested in a flow sweep experiment with a shear rate range of  $0.05 \leq \dot{\gamma} \leq 500$  Hz. The values were averaged to determine the viscosity of the solution.

To measure the storage and loss moduli of the equilibrium samples, The shear modulus of these hydrogels was measured via oscillatory shear rheology using a 3 mm plate on an TA Ares-G2 rheometer, lowered just until contact with the sample resulted in a slight increase in force. Approximately 4 mm<sup>2</sup> pieces of both the equilibrium and hierarchical gel samples were tested, first with a dynamic strain sweep to determine the strain region appropriate for testing, and next with a dynamic frequency sweep from 0.1–10 rad/s.

## RPA theory and computation

A random phase approximation (RPA) model of the collective structure factors of the SOS/THF(DMF)/water system was used to obtain micro- and macro-structure spinodal curves.<sup>30,32</sup> The RPA is based on a weak inhomogeneity expansion of the free energy of the system and a mean-field approximation. With this approach, one can calculate nonideal structure factors, which can then be used to estimate spinodal points for both micro- and macrophase separation by finding wave vectors  $q$  where the structure factors diverge. In the supporting information, we provide a derivation of equations for the RPA structure factors and a description of a numerical method for solving these equations. The RPA model parameters include: the degree of polymerization of SOS  $N_p$ , the block fraction  $f_i$  of component  $i$ , and Flory–Huggins binary interaction parameters between the system components  $\chi_{ij}$ . Table 1 provides a list of parameters used in our calculations of the spinodal points. The degree of polymerization and block fractions are based on the relevant experimental values. Flory–Huggins parameters were either obtained from experimental reports in the literature, or calculated based on Hansen solubility parameters. Additional details related to the calculation of parameters are contained in the SI.

Table 1  
Parameters used in the RPA (gray shading highlights values that differ between solutions with THF and DMF)

Parameter	THF as the Solvent	DMF as the Solvent
$N_p$	4436	4436
$f_O$	0.9	0.9
$f_S$	0.1	0.1
$\chi_{O-S}$	1.17	1.17
$\chi_{O-Solvent}$	0.50	0.05
$\chi_{O-Water}$	0.17	0.17
$\chi_{S-Solvent}$	0.47	0.80
$\chi_{S-Water}$	8.24	8.24
$\chi_{Solvent-Water}$	0.23	0.32

## Two-phase/1D diffusion simulation

We use a two-phase/1D diffusion model to predict solvent/water exchange and thereby calculate the “concentration trajectory” that the hydrogel fiber traverses on the ternary phase diagrams predicted by the RPA. The model consists of a fiber phase and a bath phase, and we assume constant total density, incompressibility, constant diffusivities in each phase, and no convection. Mass is free to exchange between the phases and the fiber can swell or de-swell accordingly. The resulting equations (given in detail in the SI) include diffusion equations for SOS and water in the fiber phase, diffusion equations for SOS and THF/DMF in the bath phase, and a mass balance equation that determines the location of the interface between the phases. The diffusion model contains parameters (given in the SI) for the various diffusivities of the components in each phase and the initial concentrations of each phase. We solve the model via a finite difference method using a custom-written code in Python. Additional details relating to the model equations, their derivation, model parameters, and the numerical calculations are provided in the SI.

## Declarations

## Data Availability

The data supporting the findings of this work are available in the article and the Supporting Information and deposited in ScholarSphere repository with the identifier XX.

## Acknowledgements

The research was supported by the National Science Foundation through the DMREF program (CMMI 2119717). X-ray scattering experiments were performed at the National Synchrotron Light Source II (NSLS II) facility located at sector 11-BM of Brookhaven National Lab. NSLS II is a US Department of Energy (DOE) Office of Science user facility operated for the DOE Office of Science under contract number DE-SC0012704. The authors would like to acknowledge Dr. Masafumi Fukuto and Dr. Ruipeng Li for helping to run X-ray scattering experiments at BM-11. The authors would also like Dr. Missy Hazen and Dr. John Cantolina at the Pennsylvania Huck Institute of Materials for assistance in cryo-milling and cryo-SEM characterization of hydrogel cross-sections.

## Author information

Authors and Affiliations

**Department of Materials Science and Engineering at the Pennsylvania State University, University Park, PA, USA**

Elisabeth C. Lloyd, Robert J. Hickey

**Department of Chemical Engineering, Brigham Young University, Provo, UT, USA**

Rami Alhasan, Douglas R. Tree

**Department of Macromolecular Science and Engineering, Case Western Reserve University, Cleveland, OH, USA**

Sujata Dhakal, Svetlana Morzova

## Author Contributions

E.C.L and R.J.H conceived the research. E.C.L synthesized, prepared, and characterized the hydrogels. R.A. and D.R.T. developed the model and produced the computational results. S.D. and S.M. conducted SALS experiments and provided analysis of the data. R.J.H. supervised the research. E.C.L., R.A., D.R.T., and R.J.H wrote the manuscript. All authors contributed to the analysis and discussion of the data.

Corresponding author: Robert J. Hickey, [rjh64@psu.edu](mailto:rjh64@psu.edu)

## Competing Interests

The authors declare no competing interests.

## References

1. Eder, M., Amini, S. & Fratzl, P. Biological composites-complex structures for functional diversity. *Science* **362**, 543–547 (2018).
2. Meyers, M. A., McKittrick, J. & Chen, P. Y. Structural biological materials: critical mechanics-materials connections. *Science* **339**, 773–779 (2013).
3. Shin, H., Jo, S. & Mikos, A. G. Biomimetic materials for tissue engineering. *Biomaterials* **24**, 4353–4364 (2003).
4. Sheiko, S. S. *et al.* Mechanically Diverse Gels with Equal Solvent Content. *ACS Cent Sci* **8**, 845–852 (2022).
5. Lee, K. Y., Peters, M. C., Anderson, K. W. & Mooney, D. J. Controlled growth factor release from synthetic extracellular matrices. *Nature* *2000* **408:6815** **408**, 998–1000 (2000).
6. Guimarães, C. F., Gasperini, L., Marques, A. P. & Reis, R. L. The stiffness of living tissues and its implications for tissue engineering. *Nature Reviews Materials* *2020* **5:5** **5**, 351–370 (2020).
7. Lu, P., Weaver, V. M. & Werb, Z. The extracellular matrix: a dynamic niche in cancer progression. *J Cell Biol* **196**, 395–406 (2012).
8. Armiento, A. R., Stoddart, M. J., Alini, M. & Eglin, D. Biomaterials for articular cartilage tissue engineering: Learning from biology. *Acta Biomater* **65**, 1–20 (2018).
9. Shin, H., Jo, S. & Mikos, A. G. Biomimetic materials for tissue engineering. *Biomaterials* **24**, 4353–4364 (2003).
10. Slaughter, B. V., Khurshid, S. S., Fisher, O. Z., Khademhosseini, A. & Peppas, N. A. Hydrogels in Regenerative Medicine. *Adv Mater* **21**, 3307 (2009).
11. Sakai, T. *et al.* Design and fabrication of a high-strength hydrogel with ideally homogeneous network structure from tetrahedron-like macromonomers. *Macromolecules* **41**, 5379–5384 (2008).
12. Cai, S., Niu, B., Ma, X., Wan, S. & He, X. High strength, recyclable, anti-swelling and shape-memory hydrogels based on crystal microphase crosslinking and their application as flexible sensor. *Chemical Engineering Journal* **430**, 132957 (2022).
13. Kim, J., Zhang, G., Shi, M. & Suo, Z. Fracture, fatigue, and friction of polymers in which entanglements greatly outnumber cross-links. *Science (1979)* **374**, 212–216 (2021).
14. Lin, S. *et al.* Anti-fatigue-fracture hydrogels. *Sci Adv* **5**, (2019).
15. Appel, E. A., del Barrio, J., Loh, X. J. & Scherman, O. A. Supramolecular polymeric hydrogels. *Chem Soc Rev* **41**, 6195–6214 (2012).
16. Gong, J. P. Why are double network hydrogels so tough? *Soft Matter* **6**, 2583–2590 (2010).
17. You, F., Wu, X. & Chen, X. 3D printing of porous alginate/gelatin hydrogel scaffolds and their mechanical property characterization. <http://dx.doi.org/10.1080/00914037.2016.1201830> **66**, 299–

- 306 (2016).
18. Lang, C. *et al.* Solvent-non-solvent rapid-injection for preparing nanostructured materials from micelles to hydrogels. *Nat Commun* **10**, 3855 (2019).
  19. Lang, C. *et al.* Nanostructured block copolymer muscles. *Nature Nanotechnology* **2022 17:7** **17**, 752–758 (2022).
  20. Lang, C., Kumar, M. & Hickey, R. J. Influence of block sequence on the colloidal self-assembly of poly(norbornene)-*block*-poly(ethylene oxide) amphiphilic block polymers using rapid injection processing. *Polym Chem* (2019) doi:10.1039/C9PY00954J.
  21. Trotter, J. A. & Purslow, P. P. Functional morphology of the endomysium in series fibered muscles. *J Morphol* **212**, 109–122 (1992).
  22. Guo, C. & Bailey, T. S. Highly distensible nanostructured elastic hydrogels from AB diblock and ABA triblock copolymer melt blends. *Soft Matter* **6**, 4807–4818 (2010).
  23. Mai, Y. & Eisenberg, A. Self-assembly of block copolymers. *Chem Soc Rev* **41**, 5969–5985 (2012).
  24. Yu, Y., Zhang, L. & Eisenberg, A. Morphogenic effect of solvent on crew-cut aggregates of amphiphilic diblock copolymers. *Macromolecules* **31**, 1144–1154 (1998).
  25. Hickey, R. J., Haynes, A. S., Kikkawa, J. M. & Park, S. J. Controlling the self-assembly structure of magnetic nanoparticles and amphiphilic block-copolymers: From micelles to vesicles. *J Am Chem Soc* **133**, 1517–1525 (2011).
  26. Ilavsky, J. & Jemian, P. R. Irena: Tool suite for modeling and analysis of small-angle scattering. *J Appl Crystallogr* **42**, 347–353 (2009).
  27. Dhakal, S., Chen, Z., Estrin, D. & Morozova, S. Spatially-Resolved Network Dynamics of Poly(vinyl alcohol) Gels Measured with Dynamic Small Angle Light Scattering. *Gels* **8**, 394 (2022).
  28. Müller, M. & Abetz, V. Nonequilibrium Processes in Polymer Membrane Formation: Theory and Experiment. *Chem Rev* **121**, 14189–14231 (2021).
  29. Fredrickson, G. H. The equilibrium theory of inhomogeneous polymers.
  30. Leibler, L. Theory of Microphase Separation in Block Copolymers. *Macromolecules* **13**, 1602–1617 (1980).
  31. Hasegawa, H. Block copolymers: Generic phase behaviour compared to surfactant phase behaviour. *Curr Opin Colloid Interface Sci* **3**, 264–269 (1998).
  32. Uneyama, T. & Doi, M. Density functional theory for block copolymer melts and blends. *Macromolecules* **38**, 196–205 (2005).
  33. Tree, D. R. *et al.* Mass-transfer driven spinodal decomposition in a ternary polymer solution. *Soft Matter* **15**, 4614–4628 (2019).
  34. Tsay, C. S. & Mchugh, A. J. Mass transfer modeling of asymmetric membrane formation by phase inversion. *J Polym Sci B Polym Phys* **28**, 1327–1365 (1990).
  35. Naeimirad, M. *et al.* Recent advances in core/shell bicomponent fibers and nanofibers: A review. *J Appl Polym Sci* **135**, 46265 (2018).

36. Luo, J. *et al.* Biomimetic Strain-Stiffening Hydrogel with Crimped Structure. *Adv Funct Mater* **31**, 2104139 (2021).
37. Kamata, H., Akagi, Y., Kayasuga-Kariya, Y., Chung, U. II & Sakai, T. 'Nonswellable' hydrogel without mechanical hysteresis. *Science* **343**, 873–875 (2014).
38. Pan, J. *et al.* Hierarchical Multiscale Hydrogels with Identical Compositions Yet Disparate Properties via Tunable Phase Separation. *Adv Funct Mater* **32**, 2110277 (2022).
39. Han, L. *et al.* Tough, self-healable and tissue-adhesive hydrogel with tunable multifunctionality. *NPG Asia Materials* 2017 9:4 **9**, e372–e372 (2017).
40. Song, X. *et al.* A Novel Human-Like Collagen Hydrogel Scaffold with Porous Structure and Sponge-Like Properties. *Polymers* 2017, Vol. 9, Page 638 **9**, 638 (2017).
41. Luo, R., Wu, J., Dinh, N. D. & Chen, C. H. Gradient Porous Elastic Hydrogels with Shape-Memory Property and Anisotropic Responses for Programmable Locomotion. *Adv Funct Mater* **25**, 7272–7279 (2015).
42. Jiang, N. *et al.* Bioprinted Injectable Hierarchically Porous Gelatin Methacryloyl Hydrogel Constructs with Shape-Memory Properties. *Adv Funct Mater* **30**, 2003740 (2020).
43. Zhang, W., Zhang, K., Yan, S., Wu, J. & Yin, J. A tough and self-healing poly(L-glutamic acid)-based composite hydrogel for tissue engineering. *J Mater Chem B* **6**, 6865–6876 (2018).
44. Liu, C. *et al.* Tough hydrogels with rapid self-reinforcement. *Science* **372**, 1078–1081 (2021).
45. Cui, Y., Tan, M., Zhu, A. & Guo, M. Strain hardening and highly resilient hydrogels crosslinked by chain-extended reactive pseudo-polyrotaxane. *RSC Adv* **4**, 56791–56797 (2014).
46. Feig, V. R., Tran, H., Lee, M. & Bao, Z. Mechanically tunable conductive interpenetrating network hydrogels that mimic the elastic moduli of biological tissue. *Nature Communications* 2018 9:1 **9**, 1–9 (2018).
47. Park, N. & Kim, J. Anisotropic Hydrogels with a Multiscale Hierarchical Structure Exhibiting High Strength and Toughness for Mimicking Tendons. *ACS Appl Mater Interfaces* **14**, 4479–4489 (2022).
48. Mougín, A. *et al.* Double-Network Hydrogels with Extremely High Mechanical Strength. *Advanced Materials* **15**, 1155–1158 (2003).
49. Wang, Z. *et al.* Toughening hydrogels through force-triggered chemical reactions that lengthen polymer strands. *Science (1979)* **374**, 193 (2021).
50. Vashahi, F. *et al.* Injectable bottlebrush hydrogels with tissue-mimetic mechanical properties. *Sci Adv* **8**, (2022).

## Figures

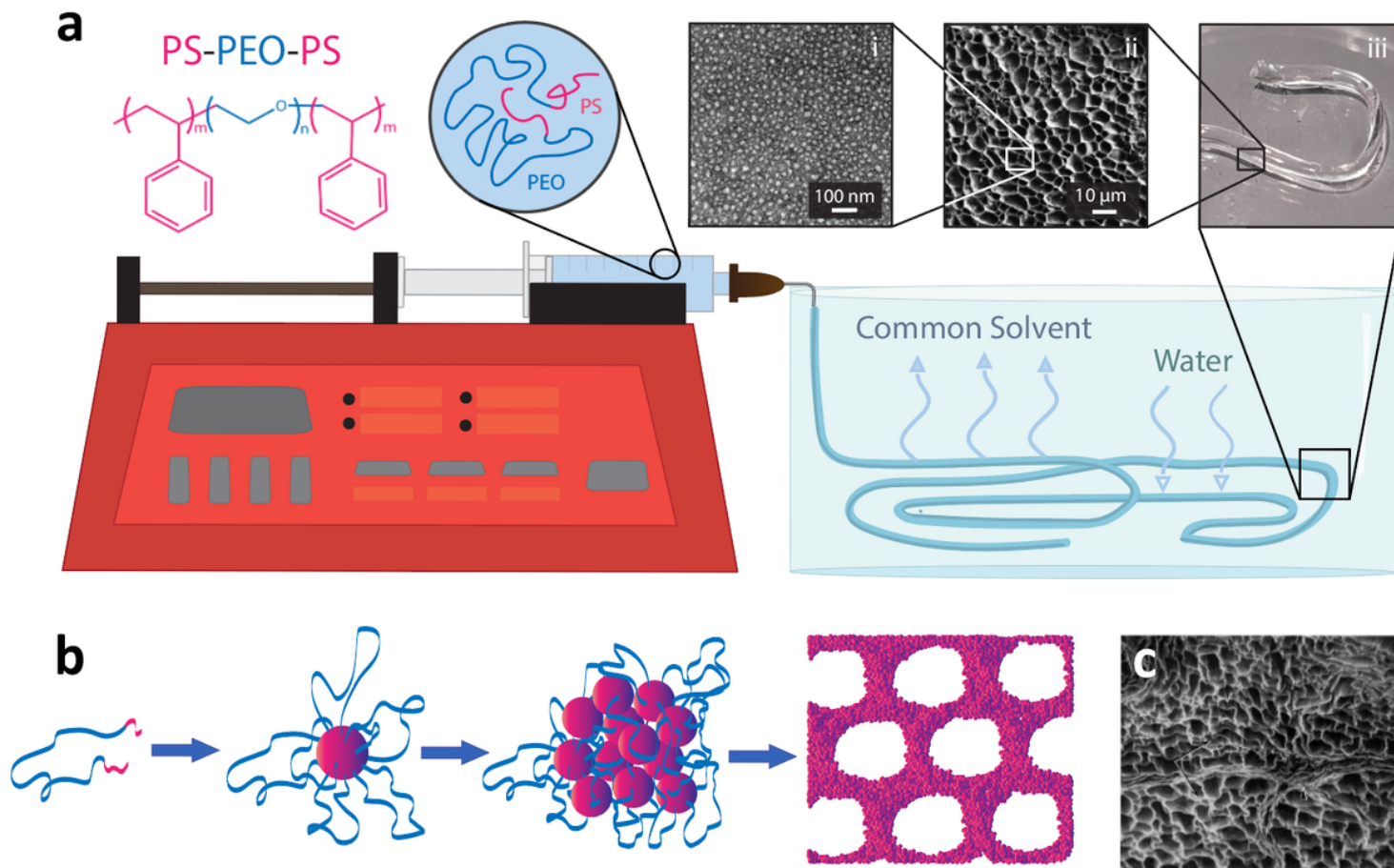


**Figure 1**

**Processing and visualization of hierarchically structured hydrogels.** a) Hydrogels exhibiting hierarchical order are prepared using a rapid injection processing method in which an amphiphilic triblock copolymer (e.g., SOS) is initially dissolved in a water miscible organic solvent and injected into water using a syringe pump. Hydrogel fibers exhibit a multiscale structure spanning many orders of magnitude where i) randomly oriented micelles organize into a network at the nanoscale that comprises ii) the walls of the water-rich cavities that form a highly aligned porous microstructure in the direction of iii) the hydrogel fiber. b) Scheme representing the different levels of ordering starting from a single triblock copolymer chain and ending with micrometer sized pores. c) Decellularized muscle tissue with natural hierarchical structure mirroring hydrogel structure with rapid injection processing. Reproduced with permission from reference 16. Copyright 2005 John Wiley and Sons.

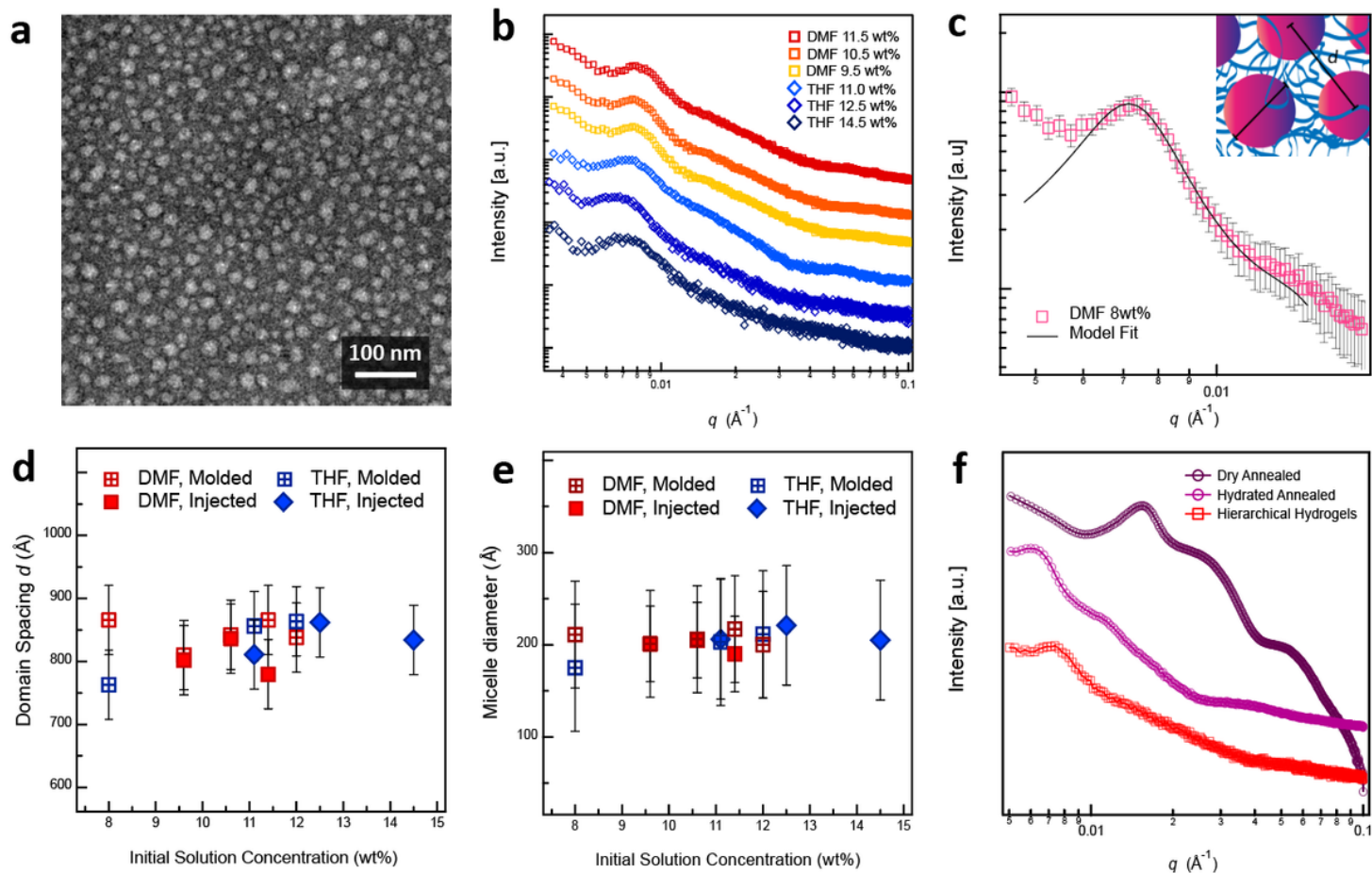


**Figure 2**

**Nanoscale characterization of hierarchical hydrogels.** a) TEM image of a dehydrated SOS microgel formed using DMF showing the micelle diameter. Disordered sphere morphology is evident in the microgel, with an estimated micelle core size of  $20 \pm 1$  nm. b) Synchrotron SAXS patterns performed on all six hydrogel samples indicating that the micelle center-to-center spacing, as indicated by the  $q^*$  value, are similar regardless of initial solution parameters (solvent, concentration). c) Example of a fitting the SAXS data with a spherical form factor and a Percus-Yevick hard sphere approximation structure factor. The model agrees with the data, but with deviation at low  $q$  due to the large-scale pore structure. d, e) Plots showing that the d) micelle diameter and e) micelle-to-micelle distance values determined from the SAXS fits are within error between different hydrogel preparation conditions. f) SAXS plots comparing the difference in the 1D scattering patterns between the hierarchical hydrogels prepared via rapid injection processing (DMF 11.5 wt% sample, shown in red in **Figure 2b** as well as **Figure 2f**), annealed SOS sample in the dry state (violet), and hydrated annealed SOS sample (magenta).

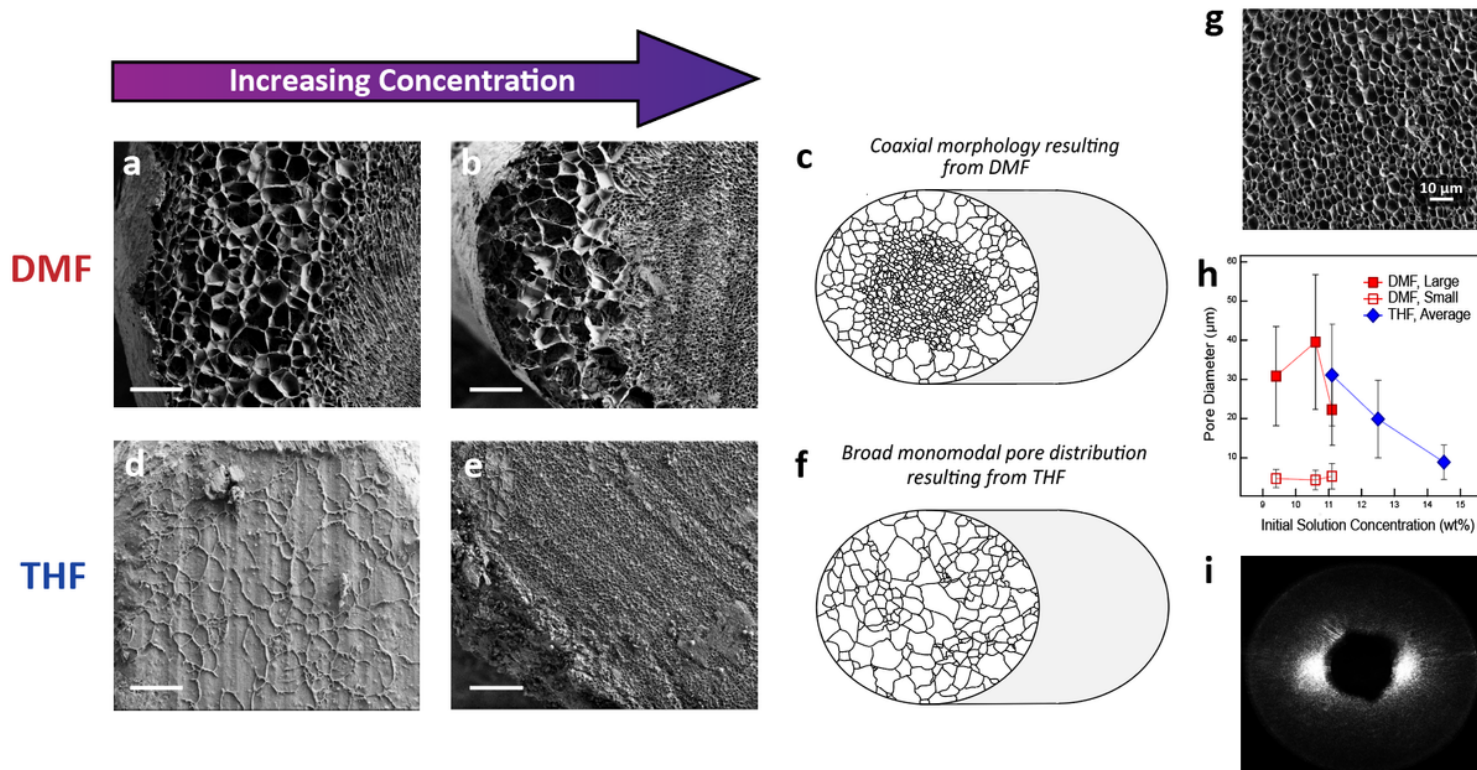


**Figure 3**

**Characterization of hydrogel fiber microstructure prepared using different solvents and concentrations.**

Cryo-SEM images of hydrogels prepared using a, b) DMF and d, e) THF show the highly porous microstructure of the hydrogel fibers. Hydrogel fibers prepared using DMF display a coaxial morphology where larger and smaller pores reside in the outer and inner regions, respectively, while the THF samples show a monomodal pore size distribution that narrows with increasing concentration. Scale bar: 100 μm. c, f) Representations of the hydrogel microstructures for DMF and THF samples. g) Higher magnification cryo-SEM image highlighting the more uniform pore size in the core region of the hydrogel fiber prepared using the 11.5 wt% polymer solution in DMF. h) Change in average pore diameter with respect to initial polymer concentration when using either THF or DMF as the solvent. The DMF samples have two different pore diameters organized in a coaxial arrangement, while hydrogels prepared with THF have an averaged pore size across the entire sample. i) SALS 2D plot for a hydrogel fiber produced using an initial solution of 12.5 wt% polymer in THF. The pattern shows a significant degree of orientation of the pores along the length of the fiber, indicating a cylindrical pore geometry.

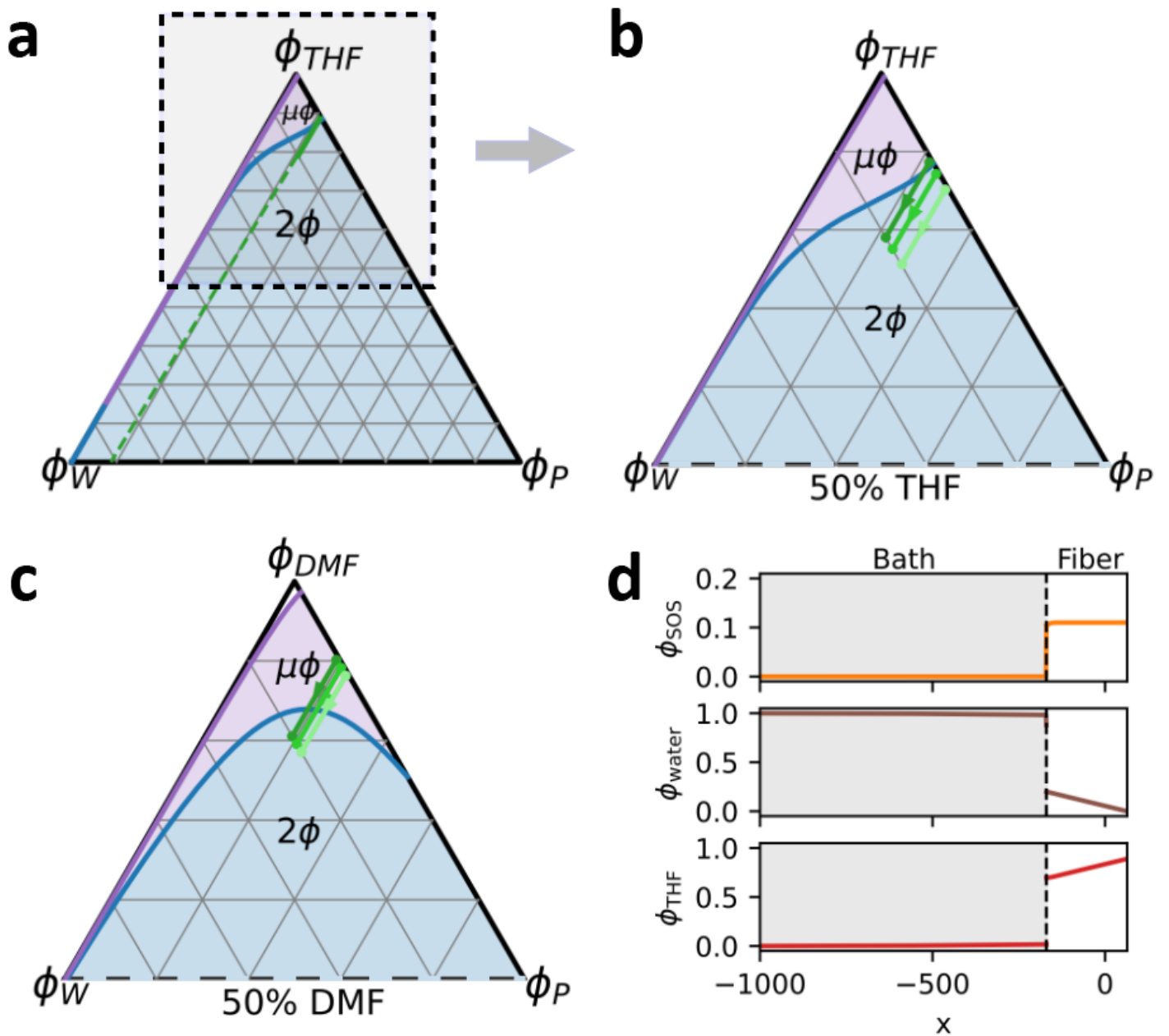
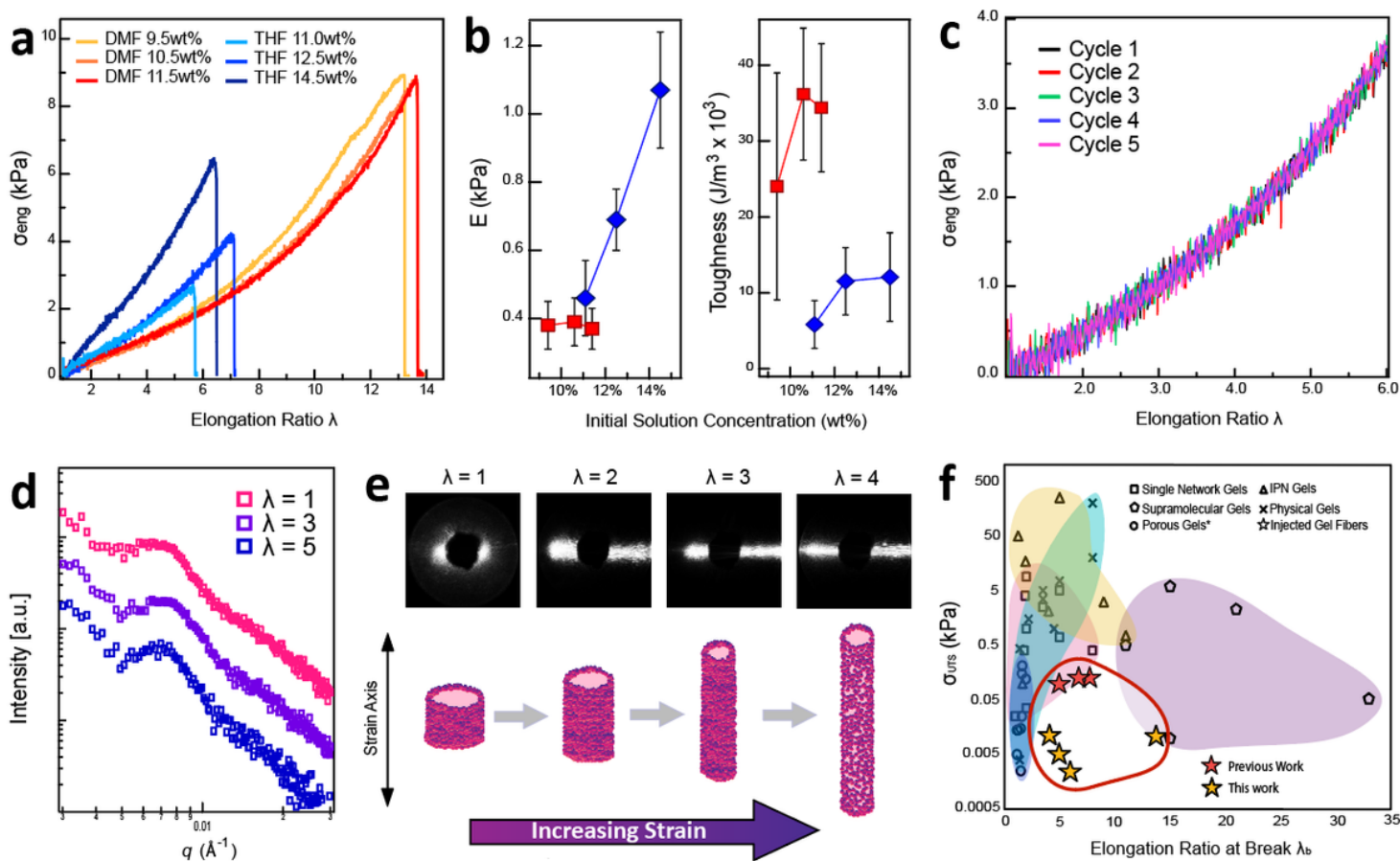


Figure 4

**Experimental validation and predicted phase diagrams to determine factors that control microstructure formation in hierarchical hydrogels.** a) A full ternary phase diagram showing microphase ( $\mu\phi$ ) and macrophase ( $2\phi$ ) spinodals of a system containing water, THF, and SOS copolymer. The dashed green line is the expected path of the average concentration inside the fiber phase during the exchange of solvents. b) The upper part of the ternary phase diagram (as indicated by **Figure 4a**) of a system containing water, THF, and SOS copolymer (limited to the region with  $\geq 50\%$  THF). The green lines show the predicted average concentration of the fiber as a function of time from the transport model in **Figure 4d** at the same concentrations used in for the samples. c) The upper part of a ternary phase diagram of water, DMF, and SOS (limited to the region with  $\geq 50\%$  DMF), with superimposed transport model prediction at the same concentrations used for the samples. d) A single time-step of a 1D transport model

of solvent/water exchange between bath and fiber at a dimensionless time  $t \approx 6 \times 10^4$  (normalized by the diffusion time). Note that a large portion of the water bath has been omitted from the plot. Also, an early separation end point is set (between the bath and the fiber) as we focus on the early-time behavior of the two cases (THF vs. DMF).



**Figure 5**

**Microstructure dependent mechanical properties of hierarchical hydrogels.** a) Representative stress-strain curves of hydrogel fibers prepared at different initial polymer concentrations and in different solvents, all tested at a strain rate of 3/min. DMF samples exhibit high extensibility and strain-hardening behavior. b) Plots showing the change in Young's Modulus ( $E$ ) and toughness with varying solvent and concentration. THF samples show an increase in  $E$  and toughness with increasing concentration, while DMF samples are constant and within error. c) Cyclic loading and unloading uniaxial extension curves for a hydrogel fiber prepared using DMF at 11 wt%. The hydrogel sample was elongated into the strain-hardening regime yet shows no hysteresis after 5 cycles. d) *In situ* SAXS of a hydrogel sample prepared from a 12.5 wt% THF solution. No change in the micelle center-to-center distance at an elongation ratio up to 5. e) 2D SALS plots at different elongations for a hydrogel sample prepared from a 12.5 wt% THF solution. There is an increase in pore alignment with respect to elongation. The proposed deformation mechanism for hierarchical hydrogels shows the transition from pore deformation at low strain to chain stretching at high strain. f) Ashby plot of ultimate tensile strength versus elongation at break for the reported

hierarchical hydrogels and different hydrogel systems. Hierarchical hydrogels are extremely soft and highly extendable when compared to a large set of hydrogel literature.

## Supplementary Files

This is a list of supplementary files associated with this preprint. Click to download.

- [HierarchicalGelsManuscriptSIFinal.docx](#)
- [SupportingVideo1.mp4](#)

## [Supporting Information]

### **Hierarchical, Porous Hydrogels Demonstrating Structurally Dependent Mechanical Properties**

Elisabeth C. Lloyd,<sup>a</sup> Rami Alhasan,<sup>b</sup> Sujata Dhakal,<sup>c</sup> Svetlana Morozova,<sup>c</sup> Douglas R. Tree,<sup>b</sup>  
Robert J. Hickey<sup>a,d,\*</sup>

<sup>a</sup>Materials Science and Engineering, The Pennsylvania State University, University Park, PA  
16802, USA

<sup>b</sup>Chemical Engineering, Brigham Young University, Provo, UT 84602, USA

<sup>c</sup>Macromolecular Science and Engineering, Case Western Reserve University, Cleveland, OH  
44106, USA

<sup>d</sup>Materials Research Institute, The Pennsylvania State University, University Park, PA 16802,  
USA

\*Corresponding author: [rjh64@psu.edu](mailto:rjh64@psu.edu)

## Table of Contents

- 1. Synthesis and Characterization of Block Copolymers**
- 2. Polymer Solution Viscosity Measurements**
- 3. Production of Hydrogels**
  - a) Hierarchical Fibers from Injection*
  - b) Hydrogels Prepared from Mold Immersion*
  - c) Conventional Physical Hydrogels as a Control*
- 4. Hydrogel Swelling Ratios**
- 5. Small-Angle X-Ray Scattering (SAXS) Data**
  - a) Data Collection*
  - b) Fitting of SAXS Data*
  - c) In Situ SAXS Under Extension*
- 6. Cryo-SEM Imaging and Microstructure Analysis**
  - a) Sample Cross-Sections at Multiple Magnifications*
  - b) Micrograph Analysis using ImageJ Software*
  - c) Small Pore Area Fraction*
  - d) Characterization of Core-Sheath Morphology*
- 7. Solvent Diffusion Coefficients Measured by Tracer Diffusion Experiments**
- 8. RPA Equations for Spinodals of Block Copolymer Solutions**
  - a) Overview of Obtaining the Spinodals via the RPA*
  - b) Formal Solution of the RPA Equations*
- 9. Solving RPA Equations to Estimate Spinodals of Block Copolymer Solutions**
  - a) Ideal Chain Structure Factors*
  - b) Numerical Method for Finding Spinodals*
- 10. Calculating and Selecting the Parameters Used to Estimate the Spinodals**
  - a) Calculating the Degree of Polymerization*
  - b) Selecting the Flory-Huggins Binary Interaction Parameters*
- 11. A Simple 1D Diffusion Model for the Solvent/Nonsolvent Exchange**
  - a) Model Description*
  - b) Initial Conditions and Parameters*
  - c) Numerical Solutions for the Diffusion Experiments*
  - d) Results of the 1D Simulations*
- 12. Critical Water Content Measurements**
- 13. Mechanical Properties**
  - a) Measuring Cross-Sectional Area*
  - b) Summary of Calculated Values*
  - c) Raw Data for Uniaxial Extension Tests*
- 14. Oscillatory Shear Rheology on Hydrogels**
- 15. Small-Angle Light Scattering Experiments**
- 16. Property Comparison with Hydrogels in the Literature**
- 17. References**

## 1. Synthesis and Characterization of Block Copolymers

The triblock copolymer, poly(styrene)-poly(ethylene oxide)-poly(styrene) (SOS) used in this study was synthesized using a previously reported sequential living anionic polymerization.<sup>1</sup> Briefly, styrene (Sigma-Aldrich) monomer was first freeze-pump-thawed and then purified twice over di-*n*-butylmagnesium (Sigma-Aldrich, 1.0 M in heptane). Purified styrene monomer was then initiated using *sec*-butyllithium (Sigma-Aldrich, 1.4 M in cyclohexane), functionalized with ethylene oxide (Sigma-Aldrich,  $\geq 99.5\%$ ) after 4 h, and finally terminated with methanol to produce the hydroxyl-terminated S homopolymer,<sup>2</sup> which was then precipitated in methanol and dried under vacuum. The purified S homopolymer was re-dissolved in tetrahydrofuran (THF) and re-initiated with potassium naphthalenide, which was prepared using a published procedure,<sup>3</sup> then purified ethylene oxide monomer was added to the reactor to form the SO diblock. A 20 mL aliquot was taken from the reactor after 24 h and terminated in sparged methanol.

After removal of the aliquot, the SOS triblock was formed by coupling the SO diblock with  $\alpha,\alpha'$ -dibromo-*p*-xylene (Sigma-Aldrich, 97%).<sup>1</sup> 10 mL of a supersaturated, air-free solution of cesium iodide (Sigma-Aldrich, 99.9%) in THF, stirred overnight at 45 °C, was added prior to the coupling agent as a source of counterions to reduce aggregation. An air-free solution of the coupling agent was similarly prepared, and the molar equivalence of one-half the number of moles of S precursor was gradually added to the reactor over a period of 4 h using a syringe pump. After 24 h, any remaining diblock was terminated with sparged methanol and precipitated in a 1:3 mixture of isopropanol and hexane. The molecular weight values for the S precursor, the diblock copolymer, and the triblock polymer as well as the individual block molecular weights, PEO volume fraction ( $f_o$ ), and dispersity are listed in **Table S1**. The molecular weight of all synthesized polymers (e.g., S-OH, SO, and SOS) were measured using a Tosoh GPC equipped

with a Wyatt multi-angle light scattering detector and THF as the mobile phase. The increase in molecular weight with each successive step of the reaction is shown in the decrease in elution time in **Figure S1**. The difference in the molecular weight between the SO diblock and S homopolymer determined the PEO block length, which was doubled to obtain the length of the PEO mid-block in the SOS triblock. The average molecular weight obtained from the SEC of the final tri-block sample is also listed. To ensure the  $dn/dc$  used in the calculations was correct, the volume fraction of PEO in the diblock and triblock samples was determined using  $H^1$  NMR in deuterated chloroform.

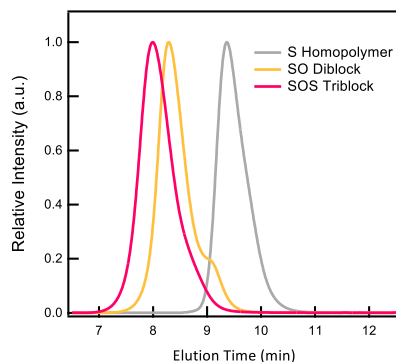


**Figure S1. Size exclusion chromatography (SEC) traces for the synthesized polymers.** There is an increase in polymer molecular weight as indicated in the decrease in elution time with successive living anionic polymerization steps: 1) S homopolymer (gray), 2) SO diblock copolymer (yellow), and 3) SOS triblock (magenta).

**Table S1:** Molecular characteristics of the polymers

<b>Polymer</b>	$M_{n, total}^a$ (kg/mol)	$M_{n,O}^b$ (kg/mol)	$M_{n,S}^b$ (kg/mol)	$f_O^c$	$D^d$
<b>S (13)</b>	13.1	-	13.1	-	1.04
<b>SO (13-96)</b>	118.2	96.2	13.1	0.90	1.04
<b>SO (13-192-13)</b>	182.4	192.4	13.1	0.90	1.05

<sup>a</sup>Number-average molecular weight ( $M_n$ ) of synthesized polymers were determined using SEC.

For the S homopolymer, previously reported  $dn/dc$  values were used.<sup>1</sup> For copolymers, the  $dn/dc$  values were calculated from polymer block weight fractions determined from <sup>1</sup>H NMR. <sup>b</sup> $M_n$  values of polymer blocks were calculated from  $M_{n, total}$  and weight fraction of different blocks obtained from <sup>1</sup>H NMR. <sup>c</sup>The O block volume fraction ( $f_O$ ) of the block copolymer was calculated using <sup>1</sup>H NMR data. The polymer block density values reported from Sigma-Aldrich, S is 1.04 g mL<sup>-1</sup> and O is 1.13 g mL<sup>-1</sup> at 25 °C, where used to calculate  $f_O$ . <sup>d</sup>Dispersity values ( $D = M_w/M_n$ ) was determined from SEC.

## 2. Polymer Solution Viscosity Measurements

The viscosity of the initial polymer solutions in both THF and DMF were measured via flow sweep experiments in the 1 – 500 Hz range at room temperature using a Discovery HR-3 Hybrid Rheometer. Parallel plate geometries measuring 2 cm for entangled solutions and 6 cm for semi-dilute solutions were used to characterize viscosity (**Figure S2a**). A solvent trap, as well as 1 mL of the organic solvent at the top of the parallel plate geometry, was used to prevent the evaporation of the solvent, which was particularly important for THF samples at higher concentrations. Due to visible aggregates forming in the 11 and 12 wt% THF samples at high shear, stepwise steady shear measurements were also performed, with the average taken at each data point the overall average viscosity was then plotted with respect to concentration (**Figure S2b**).

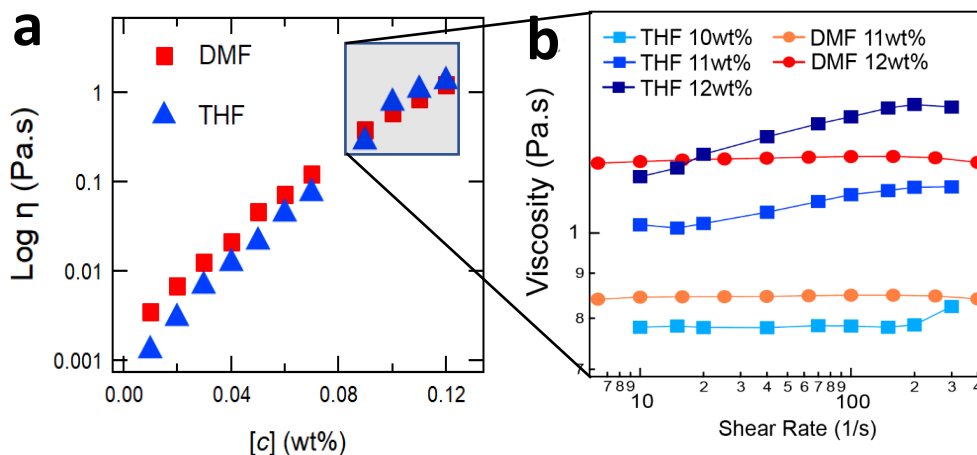


**Figure S2. Polymer solution viscosity ( $\eta$ ) versus concentration ( $c$ ) for polymer solutions prepared using THF (blue) and DMF (red).** Viscosity measurements were performed by taking the average of a flow sweep in the 5 – 500 Hz range. In the entangled regime, the viscosity of the solutions prepared using DMF and THF are similar, allowing the viscosity to be matched between two samples (shaded region).

The average viscosity from the raw data at each concentration was fit with a trendline to calculate the concentration required to match the viscosity of two samples at 1.0 Pa.s: THF 11.0 wt% and DMF 11.5 wt%. The relatively close match between the DMF and THF solutions in this regime allowed a minimal difference in concentration when matching viscosity.

### **3. Production of Hydrogels**

#### *a) Hierarchical Fibers from Injection*

Initial solutions were prepared at concentrations of 11.0, 12.5, and 14.5 wt% in THF, and 9.5, 10.5, and 11.5 wt% in DMF. The solutions were stirred at 45 °C for a minimum of 3 h to ensure total dissolution before being injected into a syringe. To remove aggregates or bubbles that appeared as a result of the transfer from vial to syringe, the syringes were heated for several minutes under a stream of warm water, sealed in Parafilm© to prevent water from entering the syringe.

Solutions were injected using a 19-gauge needle with an inner diameter of 0.686 mm at a rate of 1.00 mL/min via a syringe pump. To prevent an appreciable reduction in the concentration gradient driving diffusion of the organic solvent, a minimum ratio of 1 L of water per 1 mL of injected solution was used in all cases. Due to the proximity to the surface and lower density of the organic solvents relative to water, tweezers were used to hold the end of the fibers below the surface for several seconds, at which point enough solvent had diffused out of the hydrogels to allow them to sink. Although the fibers formed immediately on injection into the water bath, they were left in the water bath for at minimum 1 h, at which point they were transferred to 20 mL scintillation vials for storage.

*b) Hydrogels Prepared from Mold Immersion*

The influence of shear on the formation of the hydrogel nanostructure was assessed by creating hydrogels in a mold and submerging them into a water bath. Hydrogels produced using a mold were thicker and less uniform as compared to the injected hydrogel fibers.

*c) Conventional Physical Hydrogels as a Control*

Conventional SOS triblock copolymer hydrogels were prepared using a modified procedure from Guo and Bailey<sup>4</sup> to compare to hydrogels created using rapid injection processing. The SOS polymer was placed in an aluminum 4-inch dog bone mold and thermally pressed into shape at 100 psi at 150 °C. After pressing, the polymer still in the mold was transferred to a vacuum oven and annealed at 150 °C for 24 h and then cooled to room temperature. Once at room temperature, the sample was immersed in water for 3 d. The prepared sample was then characterized via SAXS and oscillatory shear rheology for comparison with the hierarchically ordered hydrogels. A small piece of dry annealed polymer was also retained for characterization.

#### 4. Hydrogel Swelling Ratio

The fraction of polymer contributing to the mass of the hydrogel fibers was determined by weighing the hydrogels in the hydrated and dry states and dividing the former by the latter. The hierarchical hydrogel fibers exhibit exceptionally high-water weight fractions compared with hydrogels prepared via conventional methods.<sup>4</sup> Furthermore, the hydrogel water weight fractions were surprisingly consistent with one another even with repetition, despite variations in the initial solution solvent and concentration, as well as hydrogel microstructure.

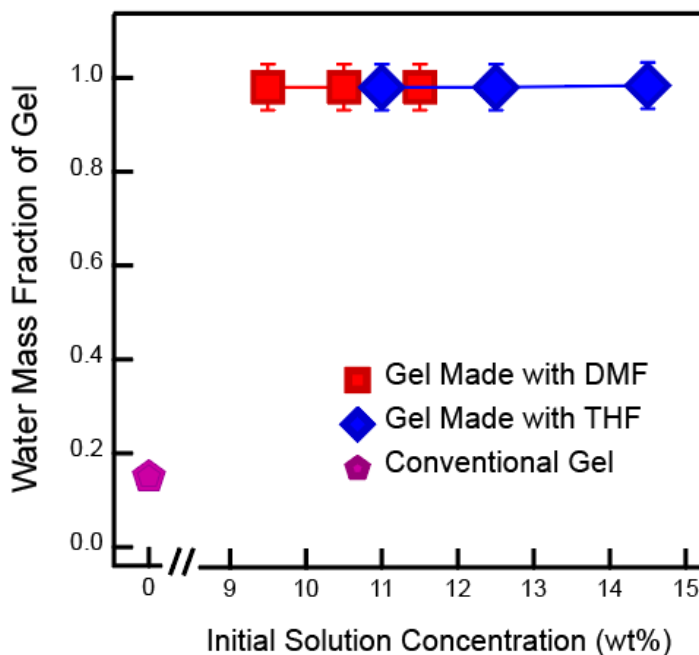


**Figure S3. Measured water weight fractions of hierarchical hydrogels.** Nearly all the DMF (red) and THF (blue) samples were 97.3% water by weight, with only the highest concentration of THF containing 97.7% water by weight. The water weight fraction of a SOS hydrogel prepared using conventional methods — as described in section 3a — is shown in pink.

## 5. Small-Angle X-Ray Scattering Data

### *a. Data collection*

Due to the high-water content of the hydrogels, a synchrotron source was required to obtain scattering data. Small-angle X-ray scattering (SAXS) measurements were performed at Brookhaven National Laboratory, National Synchrotron Light Source – II (NSLS – II), beamline 11-BM Complex Materials Scattering (CMS). The natural adhesion of the hydrogel fibers allowed them to remain in the grooves of capillary holders during measurements. Hydrogel fibers were folded over themselves to achieve better signal where necessary. Samples were exposed for 3 s using a 13.5 keV beam with a wavelength of 0.9184 Å. A sample to detector distance of 10 m was used to access the  $q$ -range 0.0044-0.03 Å<sup>-1</sup>. 2D scattering patterns were obtained using a Pilatus 2M detector. An empty beam was used to subtract the background from the hydrogel and converted to a 1D plot of intensity versus  $q$ . The background subtraction and conversion were performed for every sample measured at the beamline using the program SciAnalysis (<https://github.com/CFN-softbio/SciAnalysis>). The 1D scattering data and fits are shown for hydrogels of all concentrations for both solvents, prepared using injection (**Figure S4a**) and immersion (**Figure 4b**). Because the X-Ray scattering data shows no difference in the micelle nanostructures of the hydrogels, we infer that the formation of disordered sphere nanostructures is independent of solvent and shear-related conditions. See the next section for fitting details.

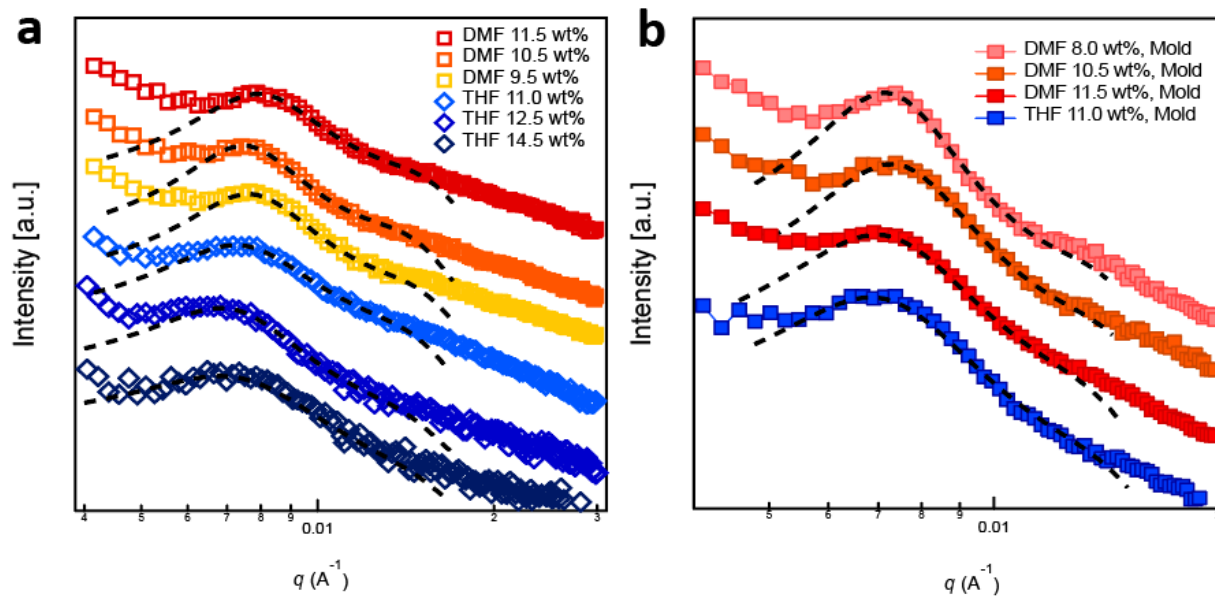


**Figure S4. 1D SAXS plots for hydrogel samples prepared using rapid injection processing and molds.** a) SAXS data for fibers formed by injecting the initial solution—solvent and polymer concentration shown in the legends—directly into water at a rate of 1 mL/min. b) Raw SAXS data for hydrogels created by injecting the initial polymer solution into a silicone mold, then immersing the mold into a water bath. SAXS data vertically shifted for clarity.

*b. Fitting of SAXS Data*

SAXS data was fit using Igor Pro with the IRENA package downloaded from Argonne National Lab.<sup>5</sup> The data was loaded into IRENA and fit with a spheroid form factor and a hard sphere structure factor derived from the Percus-Yevick approximation. The micelle diameter and standard deviation, the domain spacing (micelle center-to-center distance), and volume fraction of scatterers were used as fitting parameters. The fitting region was confined to the primary peak and immediate surroundings, as the network effects and noise at low and high  $q$ , respectively, disrupt the fit results. The micelle diameter and standard deviation from the SAXS fits agree well

with the values measured from TEM on the microgels (see **Figure 2a** in the main text), supporting the SAXS results.

The SAXS fitting parameters values indicate that the average domain spacing for all samples is  $84 \pm 3$  nm. The micelle diameters calculated by the model —  $20 \pm 4$  nm — show excellent agreement with the TEM results. Thus, the SAXS fitting results confirm there is essentially no change in micelle size, domain spacing, or volume fraction with respect to solvent or concentration. The fibers produced from the mold further corroborate these findings. Model results for domain spacing, micelle diameter, and volume fraction of scatterers are shown in **Figure S5**.

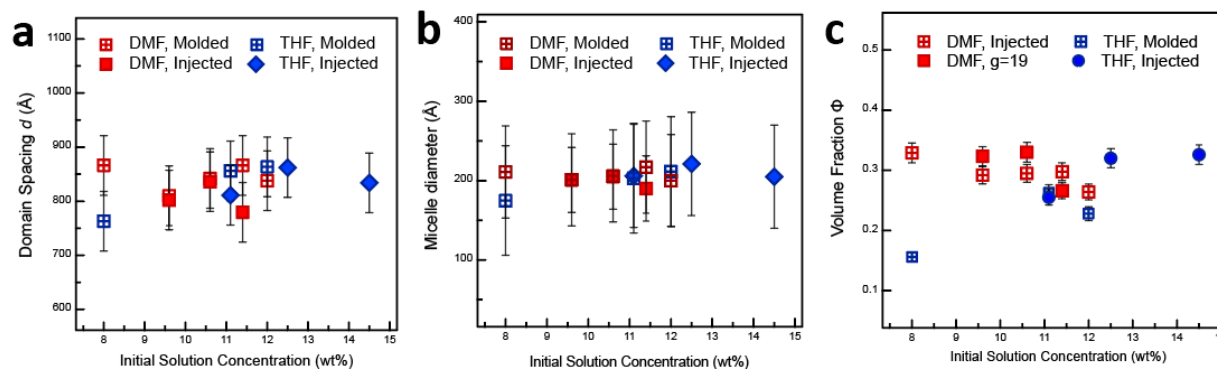


**Figure S5. Modeling fit results for hydrogel fibers that were injected directly into the water bath (solid markers) or injected into a mold and then immersed into the water bath (window markers).** Plotted a) micelle domain spacing, b) micelle diameter, and c) volume fraction of scatterers with respect to initial polymer concentration indicate that the nanoscale structural parameters are consistent across all samples.

The model was also applied to the SAXS data collected for the physically crosslinked hydrogel produced from the triblock copolymer from conventional methods (see section 3c). The domain spacing of the dry annealed sample was 43 nm, while the hydrated sample had a domain spacing of 104 nm due to swelling. Model fits show higher micelle diameter with a much larger standard deviation ( $28 \pm 13$  nm) in the conventional sample, compared with the hierarchical hydrogels. The volume fraction of scatterers calculated from the fitting parameters is similar for the conventional and hierarchical hydrogels.

*c. In Situ SAXS Under Extension*

The effect of uniaxial extension on hydrogel nanostructure was explored using in situ SAXS measurements. Samples were placed in a Linkham Modular Force Stage with Kapton windows mounted in the beam path and strained at a rate of 3/min — the same as in all mechanical property characterizations — to 1x, 2x, 3x, and 4x their initial length, consecutively. At each extension, the sample was held in place and exposed for 3 s using a 13.5 keV beam with a wavelength of 0.9184 Å. Higher extensions could not be accessed due to the decreasing diameter of the gel fibers and the damage caused by the X-ray beam. A sample to detector distance of 10 m was used to access the  $q$ -range 0.0044-0.03 Å<sup>-1</sup>. 2D scattering patterns were obtained using a Pilatus 2M detector. The 2D patterns for the hydrogel fiber with an initial solution concentration of 14.5 wt% in DMF are shown in **Figure S6** below. No change in the domain spacing is evident (see **Figure 5d** of the manuscript), but there is a slight anisotropy evident in the samples between static and tensile configurations. The relative lack of anisotropy supports the hypothesis that the pores of these samples are deforming initially and control the mechanical properties at low extensions. At high strain, stress is gradually transferred to the polymer chains bridging the

micelle cores, leading to eventual fracture. Up to moderate strain, as shown in **Figure 5** of the main text and **Figure S6** below, the nanostructure remains unchanged, with only a slight degree of anisotropy.

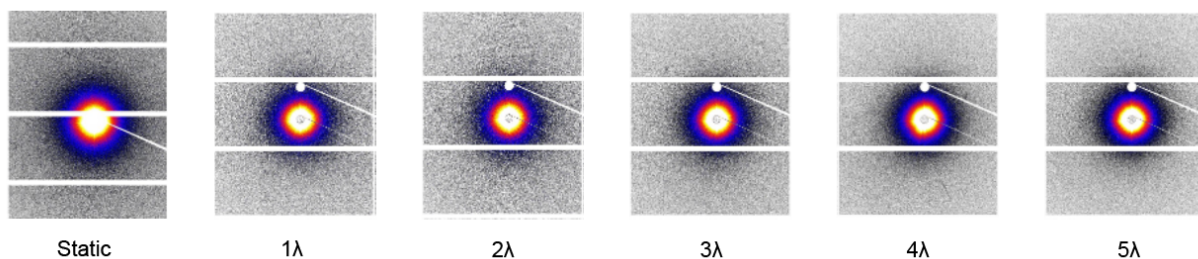


**Figure S6. 2D scattering patterns of a THF 14.5 wt% hydrogel fiber at increasing extension.** Minimal anisotropy occurring between static and tensile samples shows that the deformation of the gels up to moderate extension is dictated by the porous nanostructure rather than the micellar nanostructure.

## 6. Cryo-SEM imaging and Microstructure Analysis

### a. *Sample Cross-Sections at Multiple Magnifications*

Imaging of the fiber cross-sections was achieved by cutting the hydrogel fibers perpendicular to their length to produce 2 mm thick hydrogel discs. The sections were placed on the head of a 5 mm wide aluminum pin and placed in a cryo-microtome chamber cooled to -165 °C. After the discs had vitrified, the pins were mounted into clamps within the chamber and microtomed repeatedly until the height of the sample had been reduced by at least a half millimeter to ensure an accurate cross-section. The pins with the mounted samples were stored under liquid nitrogen. Samples were then transferred to a supercooled stud under liquid nitrogen, which was then transferred into the Cryo-SEM antechamber at -90 °C. The samples were sputter coated with a gold-palladium alloy, then transferred into the primary chamber for imaging.

Images of the hydrogel fibers are shown in **Figures S7-S12**.

## DMF 9.5 wt%

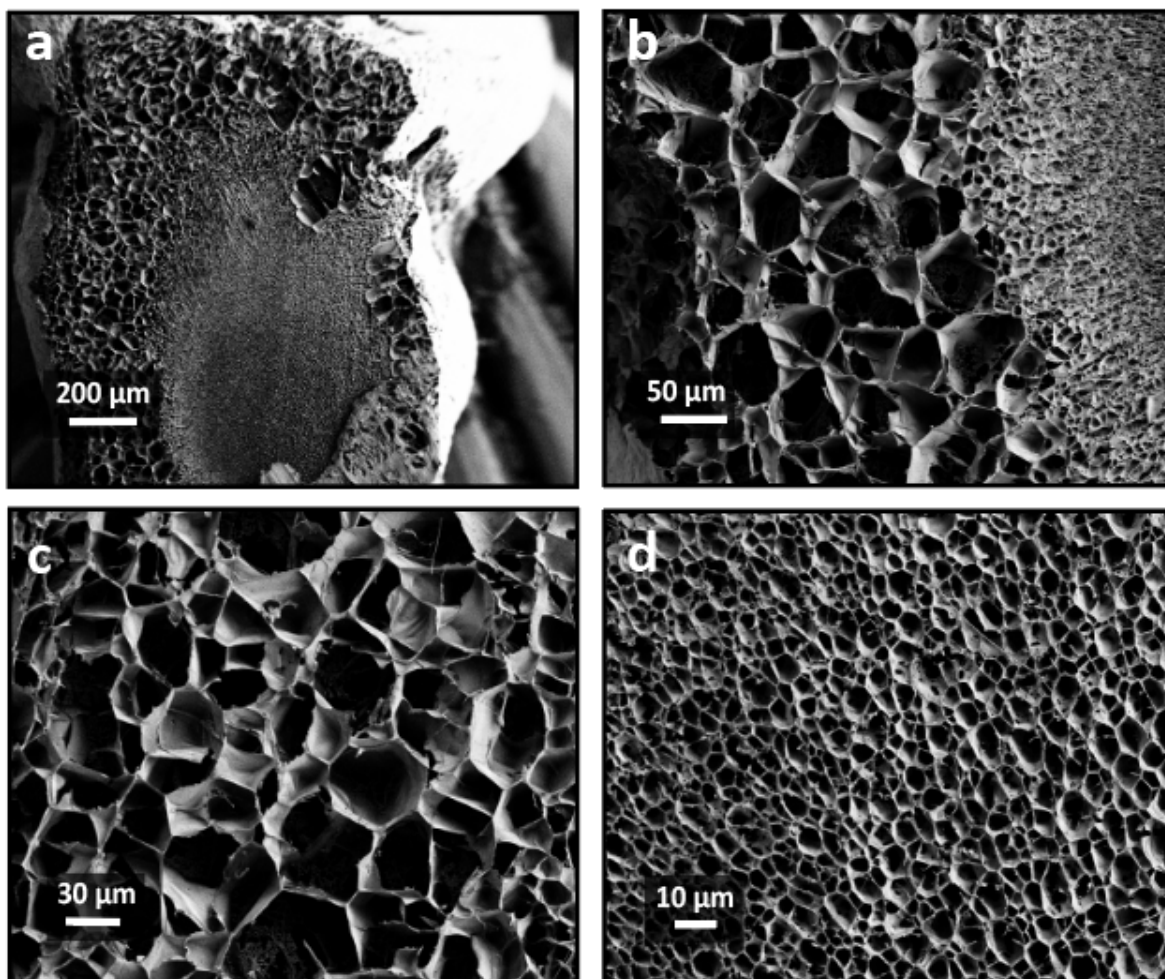


**Figure S7. The cross-section of a vitrified hydrogel fiber, produced using a 9.5 wt% polymer solution in DMF, imaged using Cryo-SEM.** a) The cross-section shows the coaxial structure with a high degree of variability in the thickness of the large pore outer sheath. b) Higher magnification of the fiber edge, showing the two distinct pore regions present in the fibers. c) High magnification of the large pore region. d) High magnification of the small pore region. Small pore region pores are much more uniform than large pore region pores.

## DMF 10.5 wt%

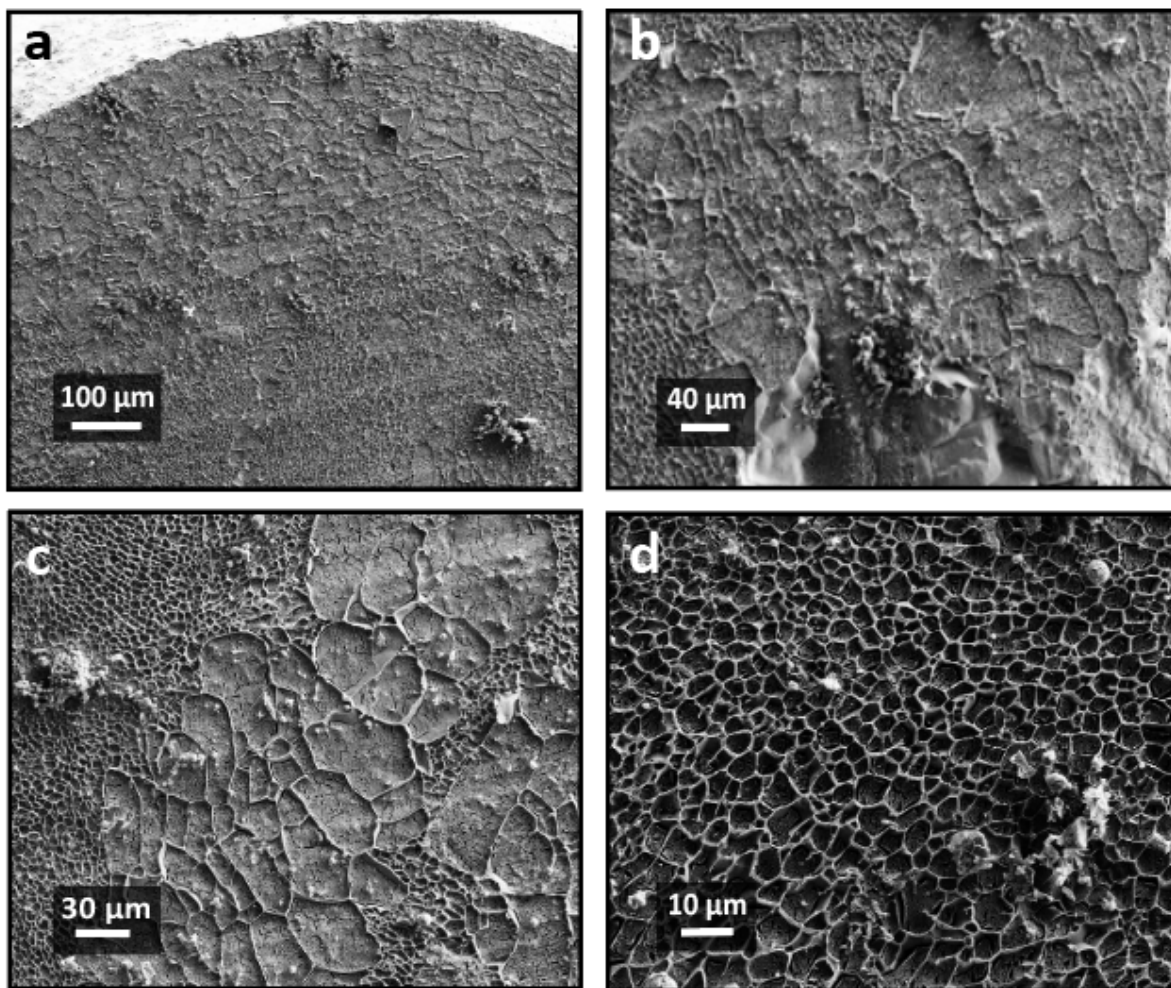


**Fig S8. The cross-section of a vitrified hydrogel fiber, produced using a 10.5 wt% polymer solution in DMF, imaged using Cryo-SEM.** Ice caps remained on large pores in the sample, reducing contrast. a) The cross-section shows the coaxial structure with less variability in the thickness of the large pore outer sheath. b) Higher magnification of the fiber edge, showing the two distinct pore regions present in the fibers. c) High magnification of the large pore outer region. d) High magnification of the small pore region.

## DMF 11.5 wt%

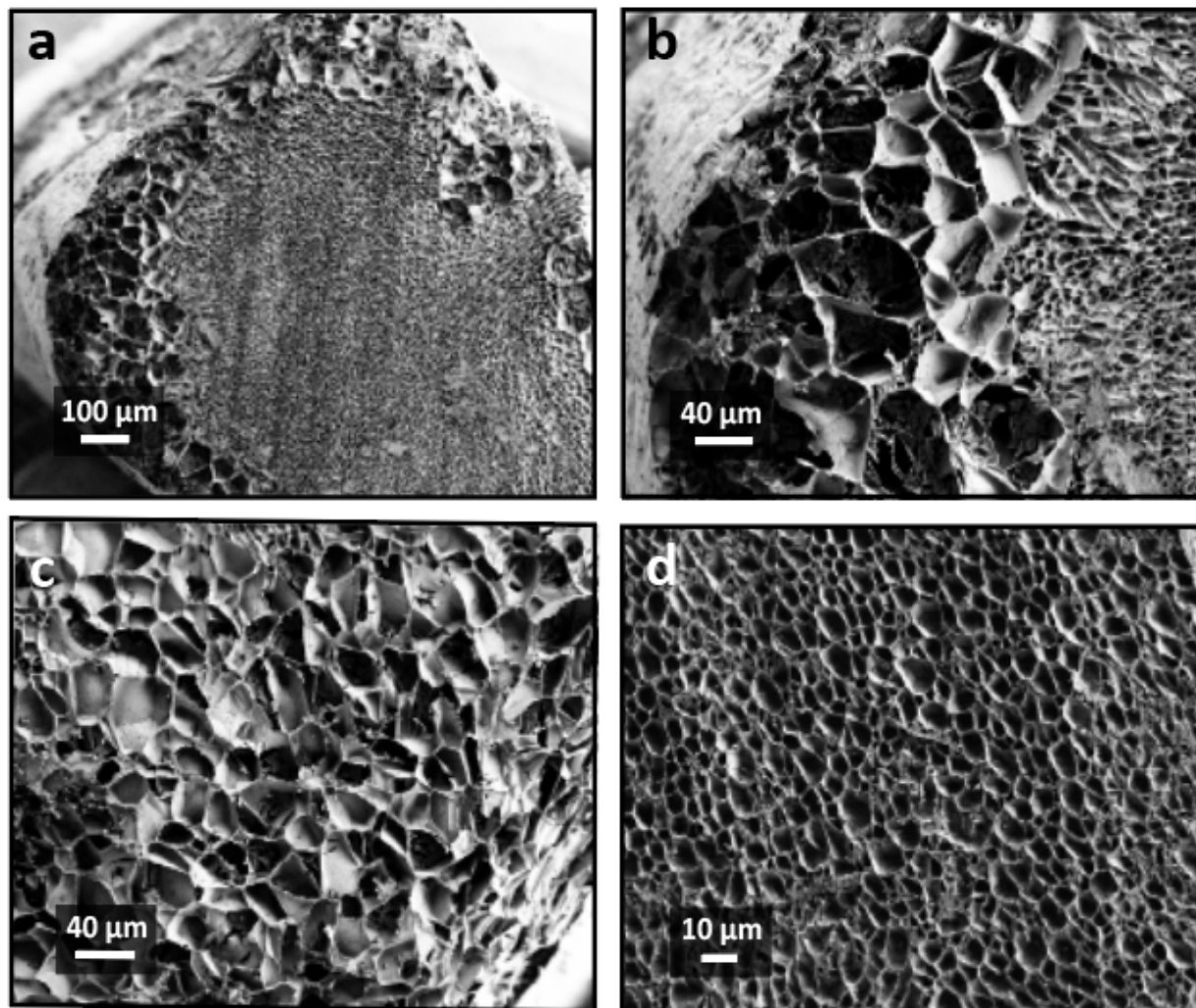


**Fig S9.** The cross-section of a vitrified hydrogel fiber, produced using a 11.5 wt% polymer solution in DMF, imaged using Cryo-SEM. a) The cross-section shows the coaxial structure is much more uniform, but the average value is well within standard deviation of the other two samples with this structure. b) Higher magnification of the fiber edge, showing the two distinct pore regions present in the fibers. c) High magnification of the large pore outer region. d) High magnification of the small pore region.

## THF 11.1 wt%

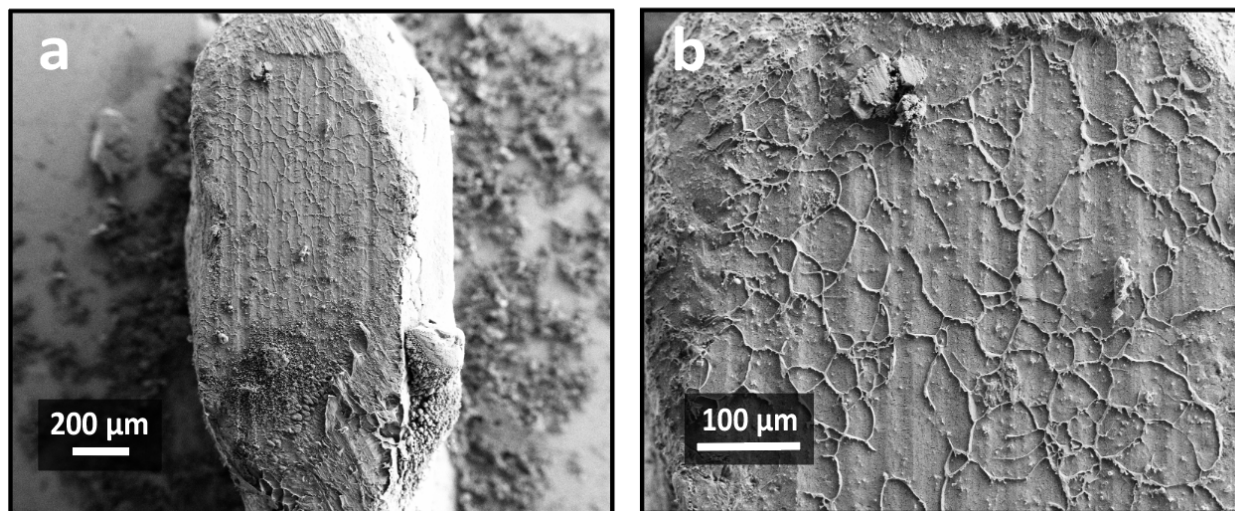


**Fig S10.** The cross-section of a vitrified hydrogel fiber, produced using a 11.1 wt% polymer solution in THF, imaged using Cryo-SEM. a) The fiber is primarily composed of a few large pores. b) Higher magnification image of the pores in this sample.

# THF 12.5 wt%

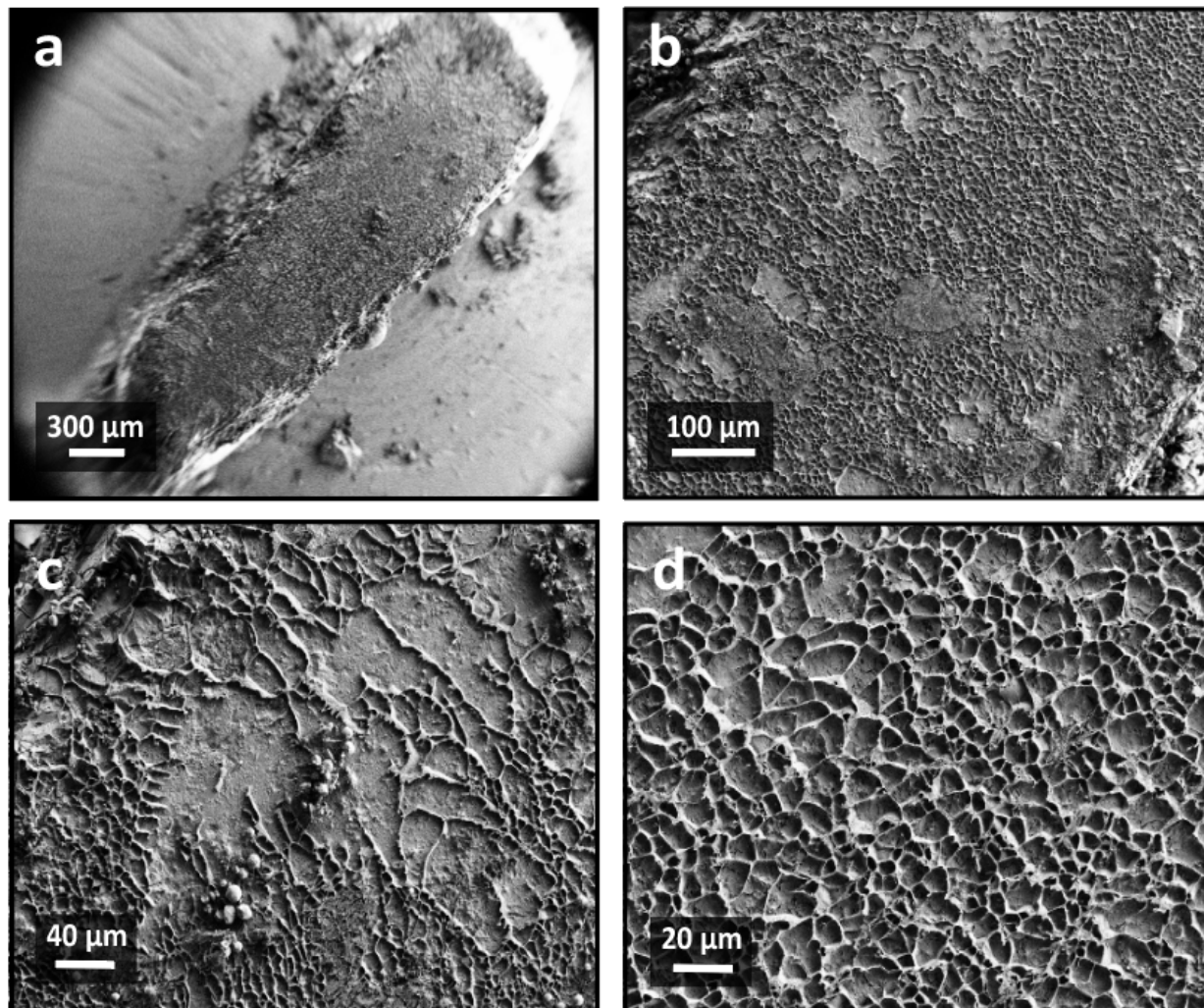


**Fig S11. The cross-section of a vitrified hydrogel fiber, produced using a 12.5 wt% polymer solution in THF, imaged using Cryo-SEM.** a) The fiber is primarily composed of a many small pores, with one lobe possessing an unusually high number of small pores. b) Large pores were also scattered sporadically throughout the sample, with c) clear boundaries between the two. d) The small pore region in this sample. All small pore regions imaged in this study showed a high degree of uniformity as well as a striking similarity in size distribution with one another.

# THF 14.5 wt%

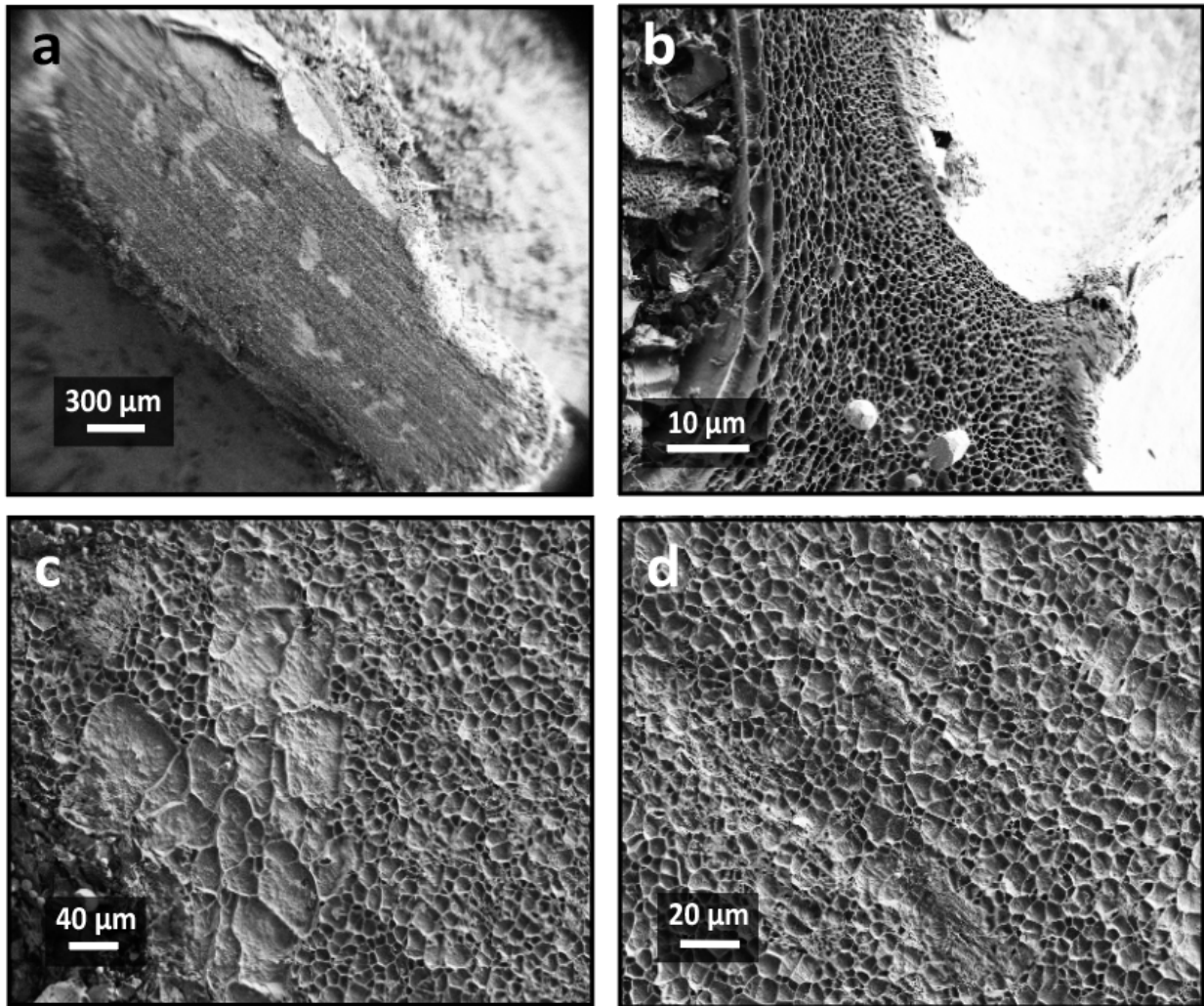


**Fig S12. The cross-section of a vitrified hydrogel fiber, produced using a 14.5 wt% polymer solution in THF, imaged using Cryo-SEM.** a) The fiber is almost entirely composed of a many small pores, with a few sporadic large pores. b) Edge of bubble inclusion withing the fibers, where the pores compressed between the bubbles appeared much stronger. This may indicate a role shear force plays in determining pore size. c) Clear boundaries between the large and d) small pores.

b. *Micrograph Analysis using ImageJ Software*

Pore sizes for the hydrogel samples were determined from cryo-SEM images that were analyzed via ImageJ software downloaded from nih.gov. First, cryo-SEM images were despeckled and converted to 8-bit binary. Then, the image threshold was set so that the pores were black regions bounded by white pore walls (**Figure S13**). Spot analysis with a minimum area of  $1 \mu\text{m}^2$  was used to eliminate static still caught within the threshold to produce measurements of the total area and Feret Diameters (the largest length between two pore walls) of each pore in the image. Some images exhibit poor contrast, and thus, the analysis was done by hand.

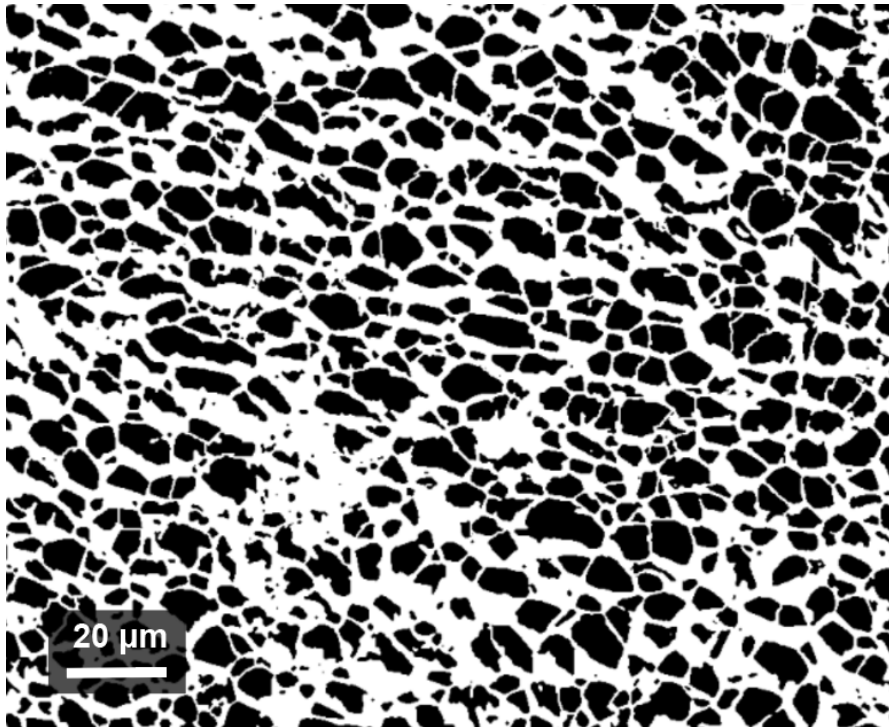


**Figure S13.** Pore image after being smoothed and converted to 8-bit binary via ImageJ software. A spot analysis with a minimum area of  $1 \mu\text{m}^2$  is used to calculate the average pore size.

### *Small Pore Area Fraction*

A rough estimate of the fraction of the cross-section area comprised of small pores was obtained by dividing the total area of the hydrogel fiber cross-section, determined using ImageJ, by the area of the small pore regions, calculated by the method described in the previous section. These values were confirmed by measuring the large pore area and performing the same calculation.

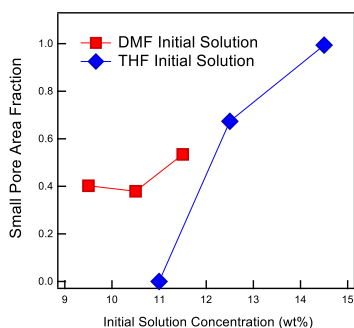


**Fig S14. The fraction of the fiber area comprised of small pores for samples produced using DMF (red) and THF (blue) as the initial organic solvents.** The small pore area fraction remains relatively consistent for the DMF samples but increases dramatically for the THF samples. The bubble inclusions in the hydrogel fiber cross-sections were not included in the calculation for the sample produced using an initial polymer solution concentration of 14.5 wt% in THF (see **Figures S11a and b**).

### *Characterization of the Core-Sheath Morphology*

The relative thickness of the outer “sheath” large-pore region in fibers possessing the coaxial morphology was measured perpendicular to the edge of the fiber at points equidistant along the perimeter of the fiber sample in Image J. As concentration increases, the diameter of the “sheath” region appears to decrease but is within error (**Figure S15**). It is possible that this indicates a trend, the existence of which is further supported by the increase in small pore area fraction seen in this morphology (see **Figure S14**). However, because variations are within error for the concentrations accessible in this study, no further conclusions may be drawn at this time.

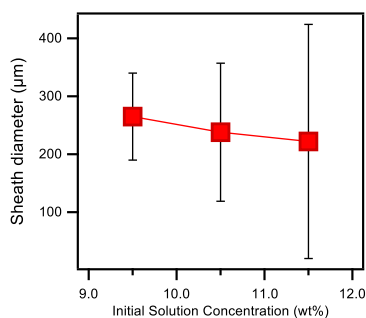


**Figure S15. A slight decrease in the thickness of the large pore “sheath” region is observed from the hydrogel cross-section micrographs.** However, the variations are within error of one another, and the potential for other parameters to affect morphology effectively prevents any conclusions from being drawn from the data at this time.

## 7. Solvent Diffusion Coefficients Measured by Tracer Diffusion Experiments

The polymer solution viscosity was held constant between two samples — THF 11.0 wt% and DMF 11.5 wt% — to isolate the effect of varying the solvent used to prepare the hydrogel. As seen in **Figure S2b**, the viscosity of the initial DMF and THF polymers solutions are in the same range, indicating that the polymer solution viscosity should have the same effect in both DMF and THF. Contrary to these expectations, the cryo-SEM images in **Figure 3a-d** show that the microstructures of the hydrogels are drastically different; THF and DMF exhibit either entirely large pores or the coaxial fiber structure, respectively.

To assess the impact of solvent diffusion, we incorporated 1 mg/mL of Eosin Y disodium salt into the initial solvents to trace the diffusion of the solvent out of solution. Briefly, 0.1 mL of the solvent/polymer/EY solutions were placed in the bottom of a quartz cuvette. At  $t = 0$ , 3 mL of water were added to the cuvette, and the increase in the maximum intensity of the EY peak was plotted with respect to time and fitted with Fick's 2<sup>nd</sup> Law of Diffusion to determine the diffusion coefficient (**Figure S16b**). Interestingly, the values were highly consistent at  $0.036 \pm 0.075$  cm<sup>2</sup>/min across solvent, polymer concentrations, and tracer concentrations, indicating that the diffusion of the solvent is determined by the gel rather than the solvent.

Tracer diffusion experiments using Eosin Y disodium salt (EY) were conducted to compare solvent diffusion coefficients between THF and DMF during hydrogel formation by tracking the increase in EY concentration during solvent exchange. **Figure S16a** shows that the EY absorption increases with time, as expected, and **Figure S16b** shows the plot of the normalized maximum absorption for solutions with respect to time. The experimental data was fitted with Fick's Second Law of Diffusion to quantify the diffusion coefficient. Interestingly, the solvent exchange rate between THF and DMF are within error, indicating that the solvent exchange rates are the same

between the two solvents. The calculated EY diffusion coefficient was constant at or around  $0.036 \pm 0.075 \text{ cm}^2/\text{min}$  for all initial polymer solution concentrations used in the study. Additionally, the diffusion coefficient does not show significant change when concentration of the tracer is increased, while keeping other parameters the same. Thus, solvent exchange rate is predicted to play a minimal role in dictating the hydrogel microstructure.

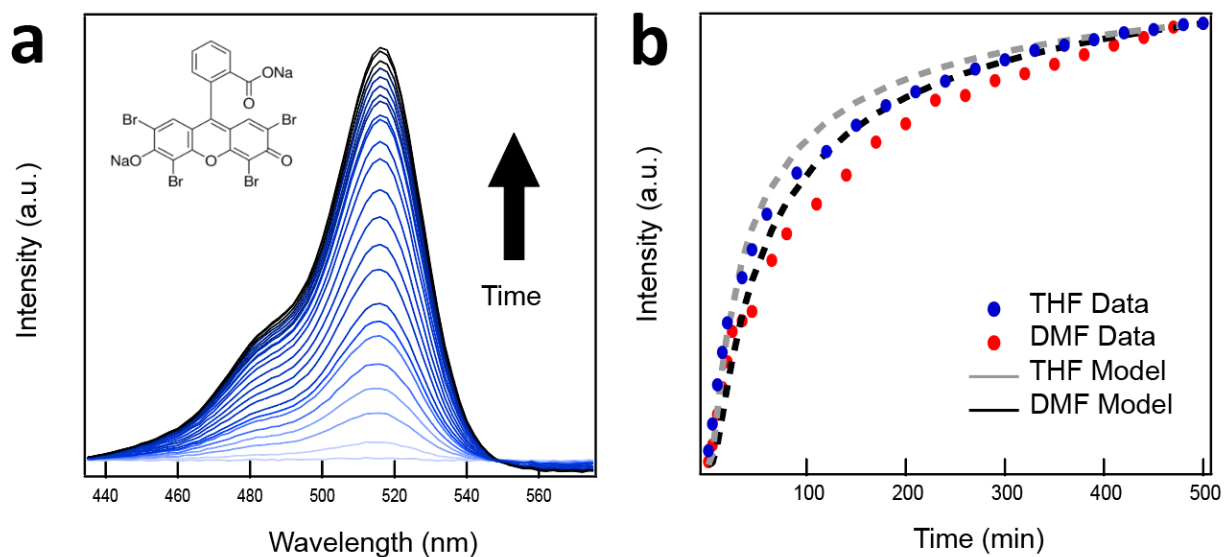


**Figure S16. Measuring EY absorbance during solvent exchange.** a) EY absorbance increases with time as EY diffuses out of the hydrogel. b) Plot of normalized intensity vs. time (min), where  $t = 0$  is the point at which water was added to the cuvette containing the solution of EY, solvent, and polymer. The data was fit with Fick's 2<sup>nd</sup> Law of diffusion to calculate the diffusion coefficient of the solvent as it diffuses from the gel.

## 8. RPA Equations for Spinodals of Block Copolymer Solutions

In this section, we provide a description of the methods for obtaining spinodals via the random phase approximation (RPA) for the response functions relevant for triblock copolymer hydrogels. Our objective is to compute spinodals for both microphase and macrophase separation behavior for mixtures of a block polymer, a good solvent, and a poor solvent. In the first section, we employ the RPA to obtain structure factors that enable the computation of spinodal points for inhomogeneous mixtures of polymers (including block copolymers, blends, and solutions).<sup>6-10</sup> [Morse2011] In the second section, we will describe a formal solution to the RPA equations for the system of interest: an incompressible solution of a block polymer, good solvent, and nonsolvent.

### a. Overview of Obtaining Spinodals via the RPA

We first define  $\varphi_i(\mathbf{r})$  to be the volume fraction of the  $i^{\text{th}}$  species at point  $\mathbf{r}$  where  $i = 1, 2, \dots, n_b$  are the blocks of the polymer,  $i = n_b + 1$  is the good solvent, and  $i = n_b + 2$  is the bad solvent. For convenience in summation formulas, we also define  $n_s = n_b + 2$  as the total number of species. The average volume fraction of species  $i$  is given by,

$$\bar{\varphi}_i = \frac{1}{V} \int d\mathbf{r} \varphi_i(\mathbf{r}) \quad (S1)$$

and the variation of the volume fraction of the monomers about the average is given by,

$$\psi_i(\mathbf{r}) = \varphi_i(\mathbf{r}) - \bar{\varphi}_i. \quad (S2)$$

A weak inhomogeneity expansion of a statistical field theory can be manipulated to give the free energy as a functional of the density variations of the species of the mixture,<sup>6,7,9</sup> which can be expressed in Fourier space as,

$$F[\varphi_i(\mathbf{r})] = F[\bar{\varphi}_i] + \frac{k_B T}{2} \sum_i^{n_s} \sum_j^{n_s} \frac{1}{(2\pi)^d} \int d\mathbf{q} \hat{\Gamma}_{ij}(\mathbf{q}) \hat{\psi}_i(\mathbf{q}) \hat{\psi}_j(-\mathbf{q}) + \dots \quad (S3)$$

where  $k_B$  is Boltzmann's constant,  $T$  is temperature,  $\hat{\psi}_i$  is the forward Fourier transform of  $\psi_i$ ,  $\hat{\Gamma}_{ij}$  is forward Fourier transform of the so-called second vertex function,  $d$  is the dimensionality, and

$\mathbf{q}$  is the wavevector. To economize on space and improve the clarity of equations, we have dropped the explicit dependence on  $\mathbf{q}$ , but all variables should be considered in Fourier space unless otherwise indicated. The second vertex function is related to density fluctuations about the homogeneous state. Specifically, the second vertex function is given by,<sup>6,7</sup>

$$\sum_{j=1}^{n_s} \hat{\Gamma}_{ij} \hat{S}_{jk} = \delta_{ik} \quad (S4)$$

where  $\hat{S}_{jk}$  is the structure factor or density correlation function,<sup>6,7,9</sup>

$$\hat{S}_{jk} = \langle \hat{\psi}_j \hat{\psi}_k \rangle. \quad (S5)$$

An examination of **Eq. S3** shows that the second vertex function is equal to the second functional derivative of the free energy. Consequently, thermodynamic stability (i.e., a spinodal point) is determined by finding the zeros of  $\hat{\Gamma}_{ij}(\mathbf{q})$ . Furthermore, the wavevector dependence of these zeros indicate the type of phase instability. If  $\hat{\Gamma}_{ij}(\mathbf{0})$  is zero, then we have located the limit of stability of a bulk macrophase. If  $\hat{\Gamma}_{ij}(\mathbf{q}^*)$  is zero at some finite wavevector  $\mathbf{q}^*$ , then the limit of stability of a microphase separation occurs at the wavelength  $2\pi/\mathbf{q}^*$ . Alternatively, the inverse relationship between  $\hat{\Gamma}_{ij}$  and  $\hat{S}_{jk}$  in **Eq. S4** makes it possible to compute spinodals using the divergence of the structure factors rather than zeros of the second vertex function.

To obtain an explicit expression of the structure factors  $\hat{S}_{ij}$ , we again turn to a weak inhomogeneity expansion. This expansion gives a linear response relationship between the density variation  $\hat{\psi}_i$  and a conjugate external field  $\hat{U}_j$ ,<sup>6-10</sup>

$$\hat{\psi}_i = -\beta \sum_{j=1}^{n_s} \hat{S}_{ij} \hat{U}_j \quad (S6)$$

where  $\beta = 1/k_B T$ . The RPA adds an additional assumption of mean-field behavior to **Eq. S6** leading to the following combined ‘‘RPA equations’’ for a system of incompressible ideal chains and solvents,<sup>6-8</sup>

$$\hat{\psi}_i = - \sum_{j=1}^{n_s} \hat{S}_{ij}^0 \left[ \beta \hat{U}_j + \sum_{k=1}^{n_s} \beta V_{jk} \hat{\psi}_k + \beta W \right] \quad (S7)$$

where  $\hat{S}_{ij}^0$  is the structure factor for a mixture of ideal (non-interacting) chains,  $W$  is a Lagrange multiplier, and  $V_{jk}$  is a mean-field interaction potential define as,

$$V_{jk} = \begin{cases} 0 & j = k, \\ k_B T \chi_{jk} & j \neq k. \end{cases} \quad (S8)$$

In the next section, we will provide a formal solution of **Eq. S7** by eliminating the implicit dependence on  $\hat{\psi}_i$ , and manipulating the subsequent expressions to the form of the linear response function in **Eq. S6**.

### *b. Formal Solution to the RPA Equations*

In this section, we formally solve the RPA equations given in **Eq. S7** in order to obtain an expression for  $\hat{S}_{ij}$ . There are two steps to solving the RPA equations: (i) use incompressibility to solve for the Lagrange multiplier  $W$ , and then (ii) rearrange to isolate and solve for  $\hat{\psi}_i$ .

To find  $W$ , we substitute Eq. S7 into the incompressibility equation,

$$\sum_i \hat{\psi}_i = 0 \quad (S9)$$

which yields,

$$W = \frac{- \sum_i \sum_j \hat{S}_{ij}^0 [\hat{U}_j + \sum_k V_{jk} \hat{\psi}_k]}{\sum_i \sum_j \hat{S}_{ij}^0} \quad (S10)$$

and by substituting the Lagrange multiplier into **Eq. S7** with considerable rearrangements and mathematics gives RPA equations,

$$\hat{\psi}_i = - \sum_{j=1}^{n_s} \hat{S}_{ij}^{inc} \left[ \beta \hat{U}_j + \sum_{k=1}^{n_s} \beta V_{jk} \hat{\psi}_k \right] \quad (S11)$$

that no longer contain  $W$ . In **Eq. S11**, we define “incompressible” ideal structure factors,

$$\hat{S}_{ij}^{inc} = \hat{S}_{ij}^0 - \frac{(\sum_l \hat{S}_{il}^0)(\sum_k \hat{S}_{kj}^0)}{\sum_k \sum_l \hat{S}_{kl}^0}. \quad (S12)$$

We can now formally solve **Eq. S11** for  $\hat{\psi}_i$  or  $\hat{\psi}_k$ . Expanding the right-hand side and mathematical manipulations with the left-hand side gives,

$$\hat{\psi}_k = - \sum_{i=1}^{n_s} (\hat{A}_{ik}^{-1})_{ki} \sum_{j=1}^{n_s} \hat{S}_{ij}^{inc} \beta \hat{U}_j \quad (S13)$$

where  $\hat{A}_{ij}$  is a new matrix defined as,

$$\hat{A}_{ik} = \delta_{ik} + \sum_{j=1}^{n_s} \hat{S}_{ij}^{inc} \beta V_{jk}. \quad (S14)$$

Comparing **Eq. S14** to **Eq. S6**, we can finally identify the nonideal structure factor predicted by the RPA,

$$\hat{S}_{kj} = \sum_{i=1}^{n_s} (\hat{A}_{ik}^{-1})_{ki} \hat{S}_{ij}^{inc}. \quad (S15)$$

In the next section, we will introduce analytical expressions for the ideal chain structure factor  $\hat{S}_{ij}^0$  and use them to compute a numerical solution for RPA equations.

## 9. Solving RPA Equations to Estimate Spinodals of Block Copolymer Solutions

In this section, we report the modeling for an ideal chain needed to solve nonideal structure factors, and the numerical methods for estimating the spinodals for block copolymer solutions using Python. In the first section, we will show how the solution for the RPA equations derived in Section A is combined with analytical expressions for the ideal chain structure factors. In the second section, we will detail how to numerically solve these equations to compute spinodals.

a. *Ideal Chain Structure Factors*

In order to evaluate  $\hat{S}_{\kappa j}$  using **Eqs. S12, S14, and S15**, we need to specify a model and determine the ideal structure factors  $\hat{S}_{ij}^0$ . We assume that the block polymer is a standard Gaussian chain with Kuhn length  $b$ .<sup>7,9</sup> The degree of polymerization of each block is  $N_{pi}$  and  $N_p = \sum_{i=1}^{n_b} N_{pi}$  is the total degree of polymerization of the polymer. It is also convenient to define polymer block fractions  $f_{pi} = N_{pi}/N_p$ . Solvent and nonsolvent are modeled as Gaussian “chains” consisting of a single Kuhn monomer (i.e.,  $N_s = N_n = 1$ ) of length  $b$ .

In this case, the ideal structure factor matrix has the form,<sup>7,8</sup>

$$\hat{S}_{ij}^0 = \begin{bmatrix} \bar{\varphi}_p \hat{h}_{ij}(\xi_{pi}, \xi_{pj}) & 0 & 0 \\ 0 & \bar{\varphi}_s \hat{g}_D(\xi_s) & 0 \\ 0 & 0 & \bar{\varphi}_n \hat{g}_D(\xi_n) \end{bmatrix} \quad (S16)$$

where the first row and column are also matrices whose rank is equal to the number of polymer blocks,  $n_b$ . **Eq. S16** contains the polymer volume fraction  $\bar{\varphi}_p = \sum_{i=1}^{n_b} \bar{\varphi}_i$ , the solvent volume fraction  $\bar{\varphi}_s = \varphi_{n_b+1}$ , the nonsolvent volume fraction  $\bar{\varphi}_n = \varphi_{n_b+2}$ , the correlation function between polymer blocks  $\hat{h}_{ij}$  where  $\{i, j\} \in [1, 2, \dots, n_b]$ , and the Debye function  $\hat{g}_D$ . It also contains the block radius of gyration  $\xi_{pi} = N_p f_{pi} b^2 q^2 / 6$  where  $q^2 = |\mathbf{q}|^2$ , and analogous quantities for the monomeric solvent and nonsolvent  $\xi_s = \xi_n = b^2 q^2 / 6$ . The Debye function is,

$$\hat{g}_D(\xi) = \frac{2}{\xi} (e^{-\xi} + \xi - 1), \quad (S17)$$

and the correlation function for a block in a Gaussian chain is,

$$\hat{h}_{ij}(\xi_{pi}, \xi_{pj}) = \begin{cases} N_p f_{pi}^2 \hat{g}_D(\xi_{pi}) & i = j, \\ \frac{N_p f_{pi} f_{pj}}{\xi_{pi} \xi_{pj}} (e^{-\xi_{pi}} - 1)(e^{-\xi_{pj}} - 1) e^{-\frac{M_{ij} b^2 q^2}{6}} & i \neq j. \end{cases} \quad (S18)$$

The quantity  $M_{ij}$  is the shortest path (in monomer units) connecting the end of the  $i^{th}$  polymer block to the start of the  $j^{th}$  block.

*b. Numerical Method for Finding Spinodals*

In this section, we outline the numerical procedure by which we solve for the spinodals. There are three steps to obtaining spinodal curves:

- 1- Specify the model parameters.
- 2- Evaluate  $\hat{S}_{kj}(\mathbf{q})$ .
- 3- Find the values of  $\mathbf{q}$  where  $\hat{S}_{kj}(\mathbf{q})$  diverges as a function of the system parameters of interest (e.g., volume fractions  $\varphi_i$  or Flory interaction parameters  $\chi_{ij}$ ).

We will briefly discuss the details of each step in turn.

The first step involves choosing parameters for a model solution of interest. In the main manuscript for example, we provide a table of parameters for a system consisting of a good solvent, a nonsolvent, and a linear ABA triblock polymer. The parameters that need to be specified are:  $N_p, f_A, f_B, \chi_{AB}, \chi_{AS}, \chi_{AN}, \chi_{BS}, \chi_{BN},$  and  $\chi_{SN}$ .

Next, structure factors  $\hat{S}_{kj}(\mathbf{q})$  are numerically calculated according to the formulas given in Sections II and III. First, the ideal structure factor matrix  $\hat{S}_{ij}^0(\mathbf{q})$  is evaluated using **Eq. S16**, and “incompressible” structure factors  $\hat{S}_{ij}^{inc}(\mathbf{q})$  are then evaluated using **Eq. S12**. The incompressible structure factors are used to build  $\hat{A}_{ik}(\mathbf{q})$  in Eq. S14 and then to solve for  $\hat{S}_{kj}(\mathbf{q})$  using **Eq. S15**. These operations are implemented in standard Python 3.9.7 using the Anaconda distribution. Linear algebra is accomplished using the *numpy* standard library *solve* and *lstsq* functions.<sup>11</sup> We found the latter to be useful for solutions with  $\hat{A}_{ik}$  matrices that are nearly singular.

Macrophase separations can be detected using structure factors calculated with this method. To determine macrophase spinodal points, we numerically solve for points where  $1/S_{11}(q_{zero})$  (or another structure factor) crosses zero. We define  $q_{zero} = 10^{-2}$  as a good trade-off between accurately capturing the  $q \rightarrow 0$  behavior and numerical convenience. We find zeros using *brentq*, a bracketed nonlinear solver in the *scipy.optimize* Python package.<sup>12</sup>

Microphase separations are detected in a similar manner to macrophase separations, but the relevant point is now a finite wavenumber  $q_{min}$  rather than  $q_{zero}$ . Accordingly,  $q_{min}$  is first

numerically determined using the *minimize\_scalar* function in *scipy.optimize*.<sup>12</sup> A cubic spline is subsequently fit to the minima, and the zeros of spline are determined using methods previously described. These zeros are then identified as microphase spinodal points.

Phase diagrams are constructed using the above methods by sweeping two free parameters while holding the others constant. Two common types of phase diagrams are (i) those where all of the values of  $f_{pi}$  and  $\chi_{ij}$  are held constant while sweeping  $\bar{\varphi}_p$  and  $\bar{\varphi}_s$ , and (ii) those where one concentration (e.g.,  $\bar{\varphi}_n$ ) is held constant while another (e.g.,  $\bar{\varphi}_p$ ) is varied along with one of the values of  $\chi_{ij}$ . One complication that can arise is the existence of multiple spinodal points in a given parameter sweep. This situation does not present a fundamental challenge but does require some extra care to capture all the relevant spinodal points.

## 10. Calculating and Selecting the Parameters Used to Estimate the Spinodals

### a. Calculating the Degree of Polymerization

To calculate the degree of polymerization of the block copolymer  $N_p$ , we pick poly(ethylene oxide), which has a higher block fraction  $f_o = 0.9$ , to be the reference block of our polymer block-poly(styrene)-poly(ethylene oxide)-poly(styrene) or SOS described in the main manuscript. The molecular weight  $M_p$  of this polymer is 192 kg/mol, and the densities of poly(ethylene oxide)  $\rho_o$  and poly(styrene)  $\rho_s$  are 1.27 g/mL and 1.05 g/mL, respectively. Using this information, one can estimate a block-fraction-averaged molar volume of the copolymer,

$$\tilde{V}_p = \frac{M_p}{f_o \rho_o + (1 - f_o) \rho_s} \approx 153.85 \frac{L}{mol}. \quad (S19)$$

Next, the molar volume of a repeat unit or a monomer of the reference polymer, which has a molecular weight  $M_o = 44.05$  g/mol, can be easily calculated using,

$$\tilde{V}_O = \frac{M_O}{\rho_O} \approx 34.7 \frac{mL}{mol} \quad (S20)$$

Finally, we can approximate the degree of polymerization of this copolymer using a ratio of those two molar volumes in Equation S19 and S20 as follows,

$$N_p = \frac{\tilde{V}_p}{\tilde{V}_O} \approx 4436 \quad (S21)$$

*b. Selecting the Flory–Huggins Binary Interaction Parameters*

The Flory–Huggins binary interaction parameter “ $\chi$ ” is a measure of the miscibility between different components in the system. A lower  $\chi$  value indicates a higher miscibility between components. The  $\chi$  parameters between different components are needed to calculate the structure factors as indicated by **Eq. S8**. We obtain  $\chi$  values from the experimental estimations in the literature, or we resort to Hansen solubility parameters whenever experimental values are not available.<sup>13</sup> Hansen solubility parameters provide reasonably accurate estimations of  $\chi$  values for polymeric solutions.<sup>13,14</sup> The Hansen solubility parameters depend on three types of interactions: (a) atomic dispersion, (b) polar cohesion, and (c) electron exchange (hydrogen bonding).<sup>13,14</sup> **Table S2** contains the values of the  $\chi$  parameters used in the phase diagrams in the main text. **Table S2** is similar to the one in the main manuscript, but it also provides the references used for each  $\chi$  value.

**Table S2:** The  $\chi$  parameters used in our calculations of the structure factor (the gray shading highlights the values that change by using THF vs. DMF as the solvent for the copolymer)

Parameter	THF (Solvent)	Reference	DMF (Solvent)	Reference
$\chi_{O-S}$	1.17	15	1.17	15
$\chi_{O-Solvent}$	0.50	16	0.05	17
$\chi_{O-H_2O}$	0.17	18	0.17	18
$\chi_{S-Solvent}$	0.47	13	0.80	13
$\chi_{S-H_2O}$	8.24	13	8.24	13

$\chi_{Solvent-H_2O}$	0.23	13	0.32	19
-----------------------	------	----	------	----

## 11. A Simple 1D Diffusion Model for the Solvent/Nonsolvent Exchange

In here, we provide a description of the diffusion equations used to model a solvent/nonsolvent exchange system consisting of two parts: (a) a polymeric solution film, and (b) a bad solvent (nonsolvent) bath. The equations consider only one dimension, assume no convection, and account for how the substances distribute themselves within the system. The equations can be solved numerically using finite difference methods.

### *a. Model Description*

We aim to track the diffusion and exchange of solvents using simple 1D diffusion equations for a ternary system of components without convection. Two phases in contact will be initially present in the system: (a) a solution of a polymer dissolved in a solvent (fiber phase “f”), and (b) a nonsolvent bath (bath phase “b”). In those phases, three components could be present: (1) a homopolymer “P”, (2) a solvent “S”, and (3) a nonsolvent “N”. For any phase, the diffusion flux  $j_i$  in that phase is given by,

$$j_i = D_{i\alpha} \frac{d\rho_i}{dx} \quad (S22)$$

where  $D_{i\alpha}$  is the ideal diffusivity of component  $i$  in the specified phase “ $\alpha$ ” (independent of position),  $\rho_i$  is the mass density of  $i$ , and  $x$  is the position.<sup>20</sup> If we assume no convection, then the bulk velocity is very close to zero, and the mass flux  $n_i$  will be approximately equal to the diffusion flux  $j_i$ . Only for dilute components in each phase, one can write the 1D diffusion equations without convection at constant  $\rho$  and  $D_{i\alpha}$ ,

$$\frac{dw_i}{dt} = \nabla \cdot j_i = D_{i\alpha} \frac{d^2w_i}{dx^2} \quad (S23)$$

where  $w_i$  is the mass fraction of component  $i$  in the phase, and  $t$  is the time. For incompressible systems, the mass fraction is equal to the volume fraction  $w_i = \varphi_i$ ,<sup>21</sup> and the diffusion equations become,

$$\frac{d\varphi_i}{dt} = D_{i\alpha} \frac{d^2\varphi_i}{dx^2}. \quad (S24)$$

We use **Eq. S24** to calculate  $\varphi_P$  and  $\varphi_N$  in the fiber phase and  $\varphi_P$  and  $\varphi_S$  in the bath phase at every time step. The mass fraction for the component representing the bulk in each phase can be readily calculated using the fact that the sum of volume fractions must equal one ( $\sum_i \varphi_i = 1$ ).

In order to account for the change in the interface location due to solvent/nonsolvent exchange, we start from the mass flow across the interfacial surface,

$$\dot{m}_{surface} = j \cdot A \quad (S25)$$

where  $A$  is the cross-sectional area of the interface. We use **Eq. S25** to find the change in mass of the polymeric solution phase,

$$\frac{dm_s}{dt} = \sum \dot{m}_{in} - \sum \dot{m}_{out} \quad (S26)$$

where  $\dot{m}_{in}$  is the mass flowrate into the phase and  $\dot{m}_{out}$  is the mass flowrate leaving the phase. Substituting **Eqs. S22** and **S25** into **Eq. S26** and using,

$$m_s = \rho AL \quad (S27)$$

where  $\rho$  is the total density of the phase and  $L$  is the thickness of the phase, one can change **Eq. S26** at constant  $\rho$  and  $A$  into

$$\rho A \frac{dL}{dt} = D_{Ns} \frac{d\rho_N}{dx} \cdot A - D_{Sn} \frac{d\rho_S}{dx} \cdot A - D_{Pn} \frac{d\rho_P}{dx} \cdot A. \quad (S28)$$

Dividing **Eq. S28** by  $\rho A$ , we obtain the equation that account for the change of the interface in the system,

$$\frac{dL}{dt} = D_{Ns} \frac{d\varphi_N}{dx} - D_{Sn} \frac{d\varphi_S}{dx} - D_{Pn} \frac{d\varphi_P}{dx} \quad (S29)$$

### *b. Initial Conditions and Parameters*

The binary diffusion coefficients can be approximated based on a monomer diffusion coefficient,  $D_0 = k_B T / \eta_r b$ , where  $k_B$  is Boltzmann's constant,  $T$  is the system temperature,  $\eta_r$  is a reference viscosity, and  $b$  is the Kuhn length of the polymer.<sup>22</sup> We set the temperature to 293 K, the reference viscosity to 1 cP, and the Kuhn length to 1 nm. The diffusivity of the polymer  $D_P$  in the bath phase is close to zero since we want  $\varphi_P$  to be very low at all times in that phase. However,  $D_P$  in the fiber phase is approximated to be  $1/N_p$ .<sup>22</sup> The diffusivity of the solvent  $D_S$  in the bath phase is  $D_0$  as it can easily diffuse in that phase. The diffusivity of the nonsolvent  $D_N$  in the fiber phase would be nearly zero at the beginning because  $\varphi_N$  is zero initially, but  $\varphi_N$  increases significantly with time. Thus, we pick the initial interfacial  $\varphi_N/2$  as an approximate concentration in the phase, and we use a formula for  $D_N$  that depends on  $\varphi$  and  $\chi$  from our previous publication, which results in  $D_N = 0.1334 D_0$ .<sup>22</sup>

The following table shows the initial volume fractions and diffusivities used to solve for the 1D diffusion equations in each phase of the system described earlier.

**Table S3: The initial conditions and parameters used for solving the diffusion equations.**

Parameter	Bath phase	Fiber phase
$\varphi_P$	0.00	0.11
$\varphi_N$	1.00	0.00
$\varphi_S$	0.00	0.89
$D_P/D_0$	1.0e-8	1/4436
$D_N/D_0$	-	0.1334
$D_S/D_0$	1.0	-

*c. Numerical Solution for the Diffusion Equations*

To solve the diffusion equations in **Eq. S24**, we use a central finite difference for the second-order space derivative,

$$\frac{d\varphi_i}{dt} = \frac{D_{i\alpha}}{\Delta x^2} [\varphi_{i-1} - 2\varphi_i + \varphi_{i+1}], \quad (S30)$$

and we solve the equation using the “odeint” module in the Python package “scipy.integrate” at every time step. Next, we solve for the change in thickness of the polymeric solution described by **Eq. S29** where we use a forward/backward finite difference for the first-order space derivatives,

$$\frac{d\varphi_i}{dx} = \frac{D_{i\alpha}}{2\Delta x} [-3\varphi_i + 4\varphi_{i-1} - \varphi_{i-2}], \quad (S22)$$

to calculate  $dL/dt$  and update the interface location.

#### *d. Results of the 1D Simulations*

In this section, we present the findings from our 1D simulations, depicting the temporal evolution of component concentrations. **Figure S17** displays the spatial distribution of polymer concentration at five distinct simulation points. Our chosen parameters resulted in relatively stable polymer concentration throughout the simulation, with no detectable diffusion into the nonsolvent bath.

In **Figure S18**, we observe a decrease in solvent concentration at early times, followed by a steady state once the desired interfacial separation is attained during fiber swelling. Conversely, in **Figure S19**, the nonsolvent concentration within the fiber phase increases initially, but stabilizes once the desired interfacial separation is reached. This behavior is attributed to solvent exchange across the moving interface, leading to a net influx of nonsolvent into the fiber, as evidenced by fiber swelling.

**Figure S20** presents the average concentration of components within the fiber phase, as also depicted in the ternary phase diagrams in the main manuscript. Notably, the majority of concentration changes occur during the initial stages, prior to achieving the desired interfacial separation. Once this separation is achieved, the fiber phase exhibits relatively constant concentrations as it continues to swell over time.

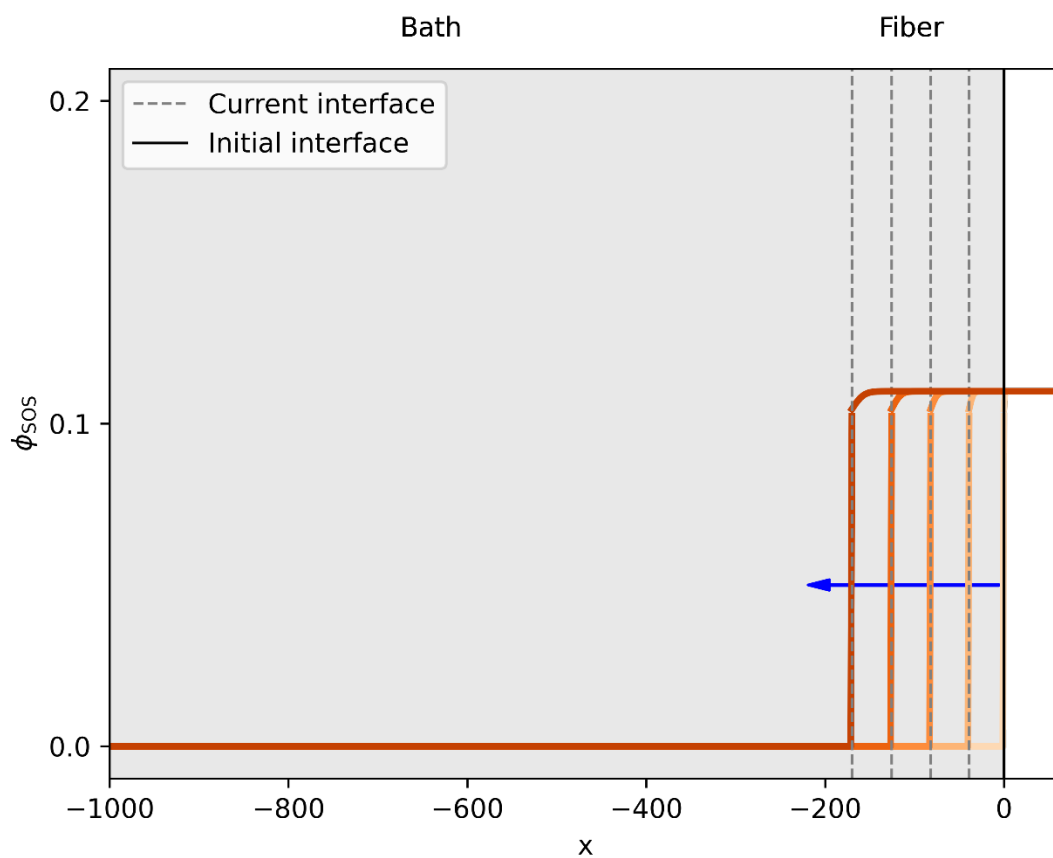


**Figure S17. The time evolution of concentration of the polymer in a system consisting of the “fiber” and the “bath”.** Initially, the fiber covers all the range where  $x > 0$  while the bath covers all the range where  $x < 0$ . The time progresses from lighter to darker orange color. The blue arrow indicates the main direction of movement of the interface between the fiber and the bath during the simulations.

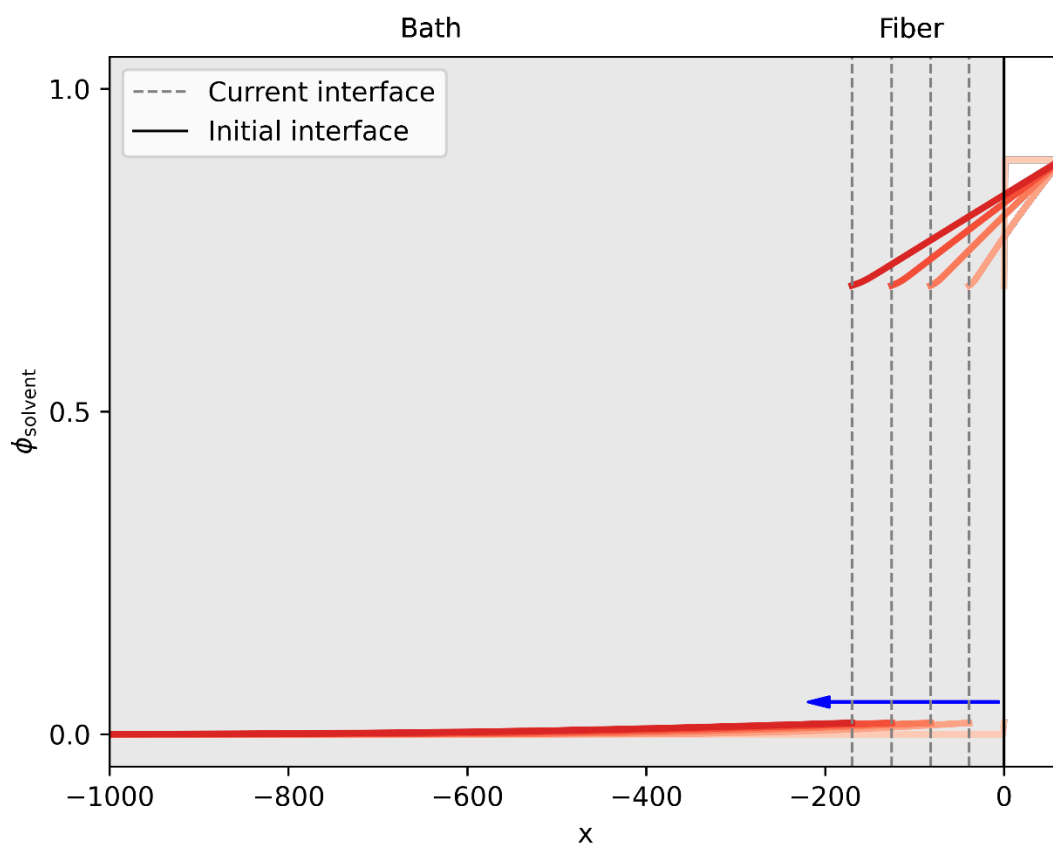


**Figure S18.** The time evolution of concentration of the solvent in a system consisting of the “fiber” and the “bath”. Initially, the fiber covers all the range where  $x > 0$  while the bath covers all the range where  $x < 0$ . The time progresses from lighter to darker red color. The blue arrow indicates the main direction of movement of the interface between the fiber and the bath during the simulations.

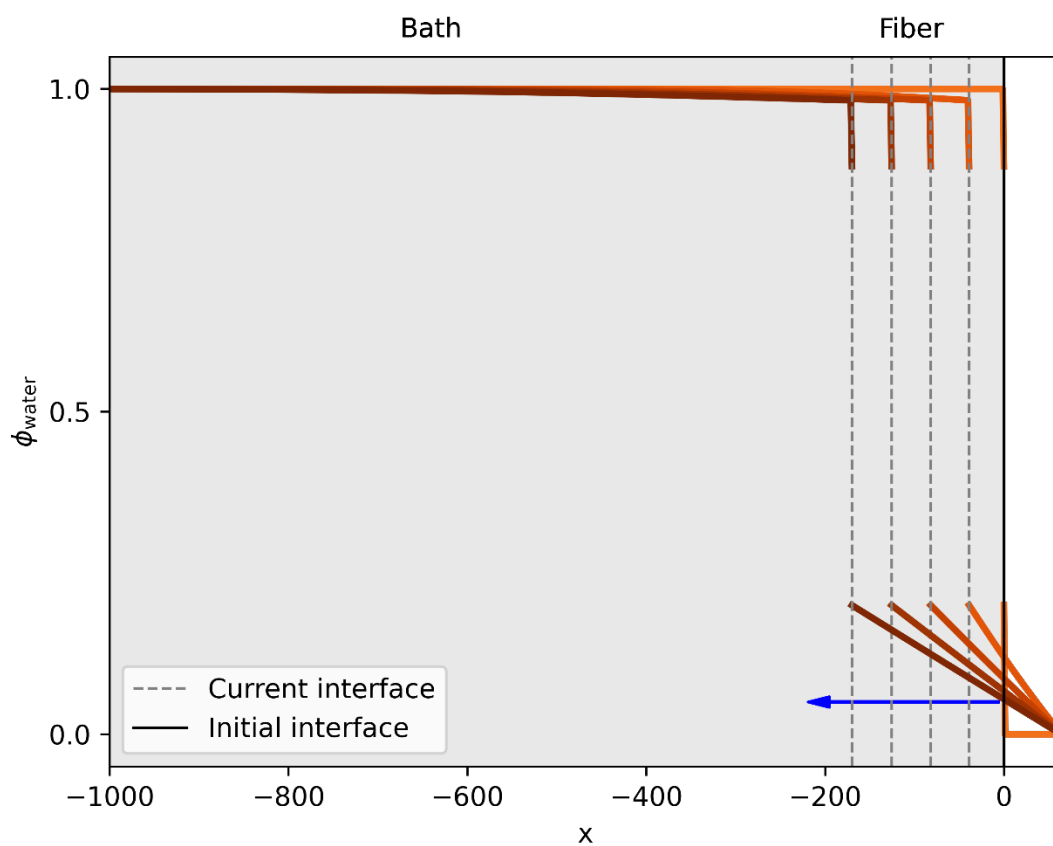


**Figure S19.** The time evolution of concentration of the nonsolvent in a system consisting of the “fiber” and the “bath”. Initially, the fiber covers all the range where  $x > 0$  while the bath covers all the range where  $x < 0$ . The time progresses from lighter to darker brown color. The blue arrow indicates the main direction of movement of the interface between the fiber and the bath during the simulations.

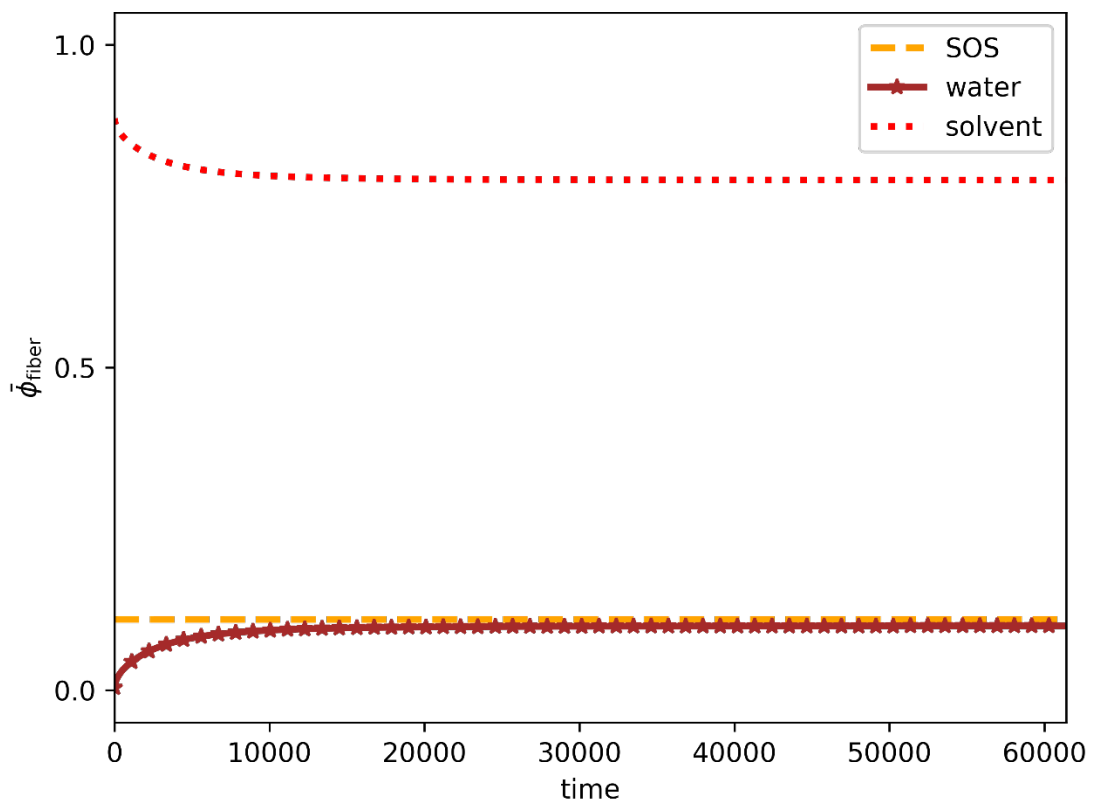


**Figure S20.** The time evolution of concentration of the average concentration of each of the three components (polymer, nonsolvent, and solvent) in the “fiber” phase.

## 12. Critical Water Content Measurements

The critical water content (CWC) — i.e., the fraction of water that induces micellization in the block copolymers — was calculated by measuring the scattering intensity of filtered, dilute solutions of the triblock copolymers in THF and DMF as the weight fraction of water in solution increased. Measurements were conducted using a Brookhaven Instruments BI-200SM Research goniometer system with a 637 nm, 30 mW laser and a 100  $\mu\text{m}$  aperture, and the solutions were filtered twice using a 0.45  $\mu\text{m}$  Teflon filter. The concentration of the initial THF and DMF solutions was selected to be 4 and 2.5 mg/mL through trial and error as the lowest concentrations producing measurable scattering. As shown in **Figure S21**, the critical water content is identical for both THF and DMF solutions, where onset and completion of micellization occurs between 7-8% water by weight. This value was shown to be unaffected by concentration.

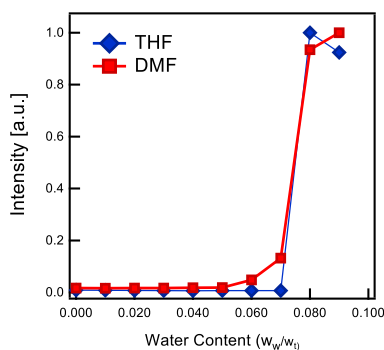


**Figure S21. Critical water content measurements in a dilute triblock copolymer solution in THF and DMF.**

## Mechanical properties

### a. *Measuring fiber cross-sectional area*

The low modulus and tensile strength of these hydrogels required a precise measurement of the cross-sectional area to accurately calculate the applied stress. Due to irregularities in the shape of the hydrogel fibers, the area was determined by taking cross-sectional slices of the hydrogel — similar to those mounted on aluminum pins for cryo-microtoming — and examining them under a bright field microscope at 2.5x magnification. Measurements were performed quickly, as the heat of the microscope began to evaporate the water within the hydrogels. At least five representative slices were used for each cross-section, and the area of the cross-sections was calculated using Image J.



**Figure S22. Example hydrogel slice used to calculate cross-sectional area for fiber samples.**

Images were obtained with a bright field microscope at 2.5x magnification.

*b. Summary of calculated values*

Due to the noise in the data, the Young's Modulus ( $E$ ) was calculated from a trendline fit to the first 100 points of data for every sample tested. The tensile strength corresponds with the maximum stress achieved by the samples. The toughness was calculated from the area under the stress-strain curve. Values are averaged for 5 to 7 samples per sample concentration. Average values and raw data are shown below.

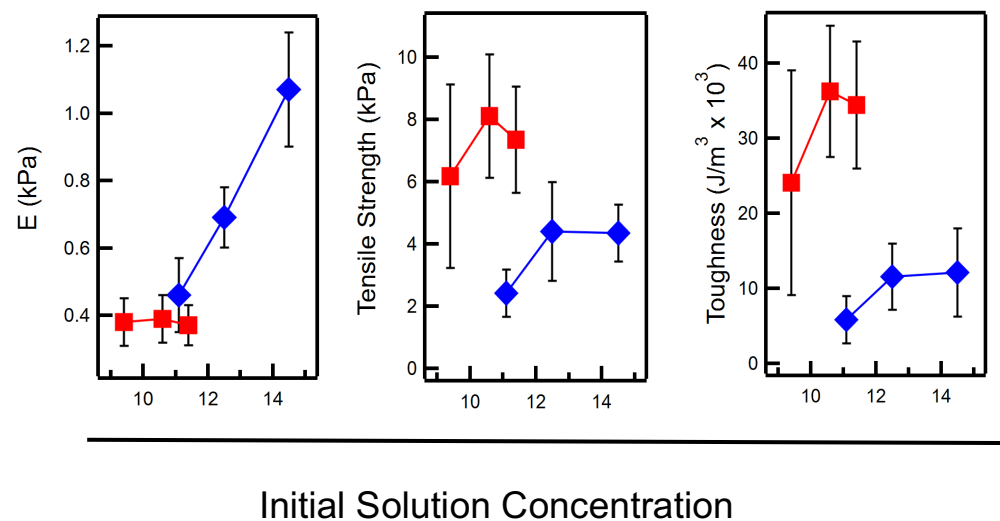


**Figure S23. Summary of measured mechanical properties.** The Young's Modulus for the DMF samples was highly consistent as the initial polymer solution increased, but the samples made with THF show a steady increase in  $E$  with concentration. The tensile strength of the samples produced with DMF were unchanging within error of one another, while the THF samples showed an increase. The variability in DMF sample tensile strength is reflected in the values calculated for toughness, but once again the values are all within error of each other. The THF samples show little variation in toughness due to the decrease in elongation with increasing initial solution concentration (see **Figure 5a**).

*c. Raw data for uniaxial extension tests*

Uniaxial extension tests were performed using spring-loaded steel grips and a 10 N load transducer on a Criterion Load frame from MTS. All samples were deformed at a rate of 3/min. In the graphs shown below, the sample data for a given initial solution condition is shown in gray, with the representative trace, which had the closest alignment to the average elongation ratio and ultimate tensile strength at break for each sample condition, highlighted in color. The color used corresponds with the samples shown in **Figure 5a**. The data for samples produced with DMF as the organic solvent shows a high degree of variability in the elongation at break at lower initial polymer solution concentrations, with some fibers failing earlier (6 times original length). Though the cause of this is unclear, it may potentially be attributed to slightly larger outer pore regions allowing cracks to propagate more easily. As initial polymer solution concentration increases for the samples produced using DMF, the elongation at break and ultimate tensile strength of the hydrogels becomes more consistent. Dips and drops in the data are attributed either to slight tearing of the fiber or to observed slippage of the hydrogel fiber from between the clamps.

THF samples showed distinct trends in mechanical properties with increasing concentration: as concentration increased, so did tensile strength and elastic modulus, consistent with results reported in previous publications where THF was used as the organic solvent. Conversely, the elongation at break decreased with increasing initial solution concentration.

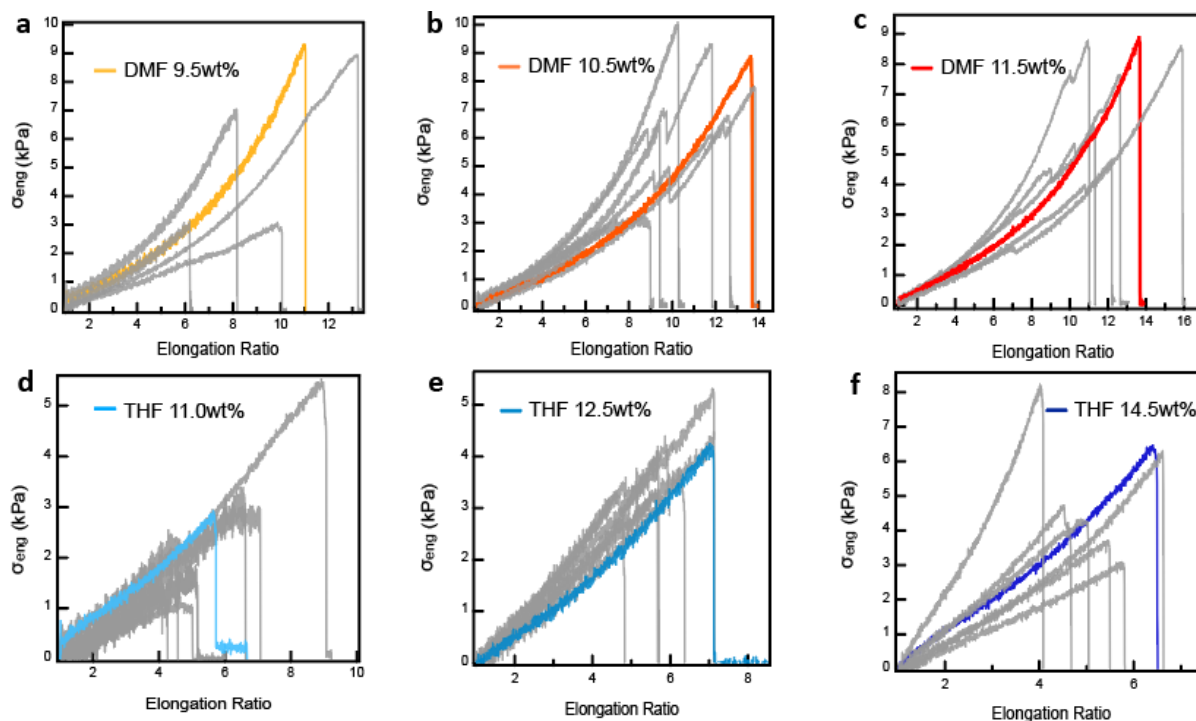


**Figure S24. Stress-strain curves generated from uniaxial tensile tests for hydrogel fibers.**

Representative samples are shown in color for a) DMF 9.5 wt%, b) DMF 10.5 wt%, c) DMF 11.5 wt%, d) THF 11 wt%, e) THF 12.5 wt%, and f) THF 14.5 wt%. A minimum of four samples were tested for each sample condition. Though DMF samples showed greater variability in mechanical properties (ultimate tensile rate) at low initial solution conditions, the average values remained consistent. In contrast, samples prepared with THF increase in both average modulus and tensile strength with concentration, but elongation at break decreases with increasing concentration.

### 13. Oscillatory shear rheology on hydrogels

While the injected fiber samples were amenable to uniaxial extension tests, the hydrogels produced using conventional methods were brittle. The shear modulus of these hydrogels was measured via oscillatory shear rheology using a TA Ares-G2 rheometer, first with a dynamic strain sweep to determine the strain region appropriate for testing, and next with a dynamic frequency sweep from 0.1-10 rad/s. Interestingly, the hydrogel fibers showed no change in the storage modulus  $G'$  with solvent or initial strain, as the storage modulus was approximately equal at both 10 and 100% strain. In contrast, the annealed “equilibrium” sample could only be tested at a strain of 2%. The lack of difference between samples is most likely due to the consistent swelling ratio for all samples.

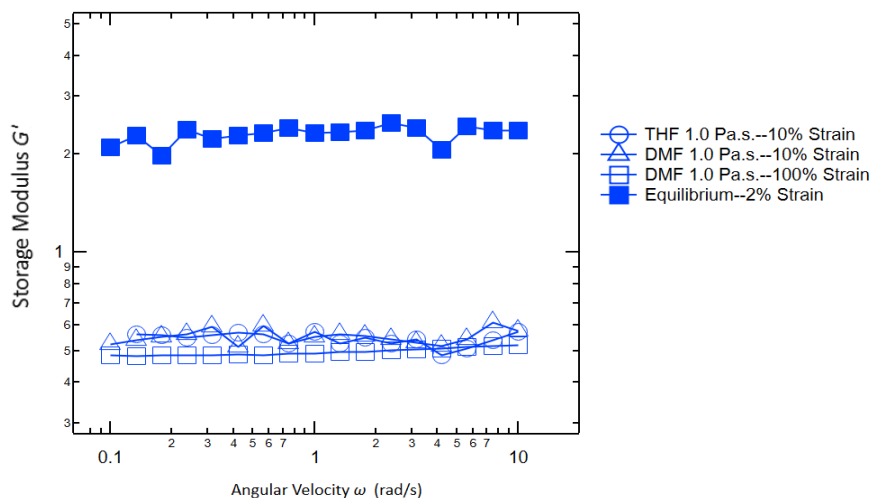


**Figure S25. Oscillatory shear rheology measurements for conventional samples and**

**injected fiber hydrogel samples.** Samples prepared through conventional methods were brittle and were thus tested at low strain. The shear modulus of the hydrogel samples was five times greater in the conventional samples than in the injected fiber samples, which is consistent with expectations. Interestingly, the injected fiber samples showed a consistent storage modulus, despite variations in both samples and strain.

## 14. Small-Angle Light Scattering Experiments

### a. Experimental Setup

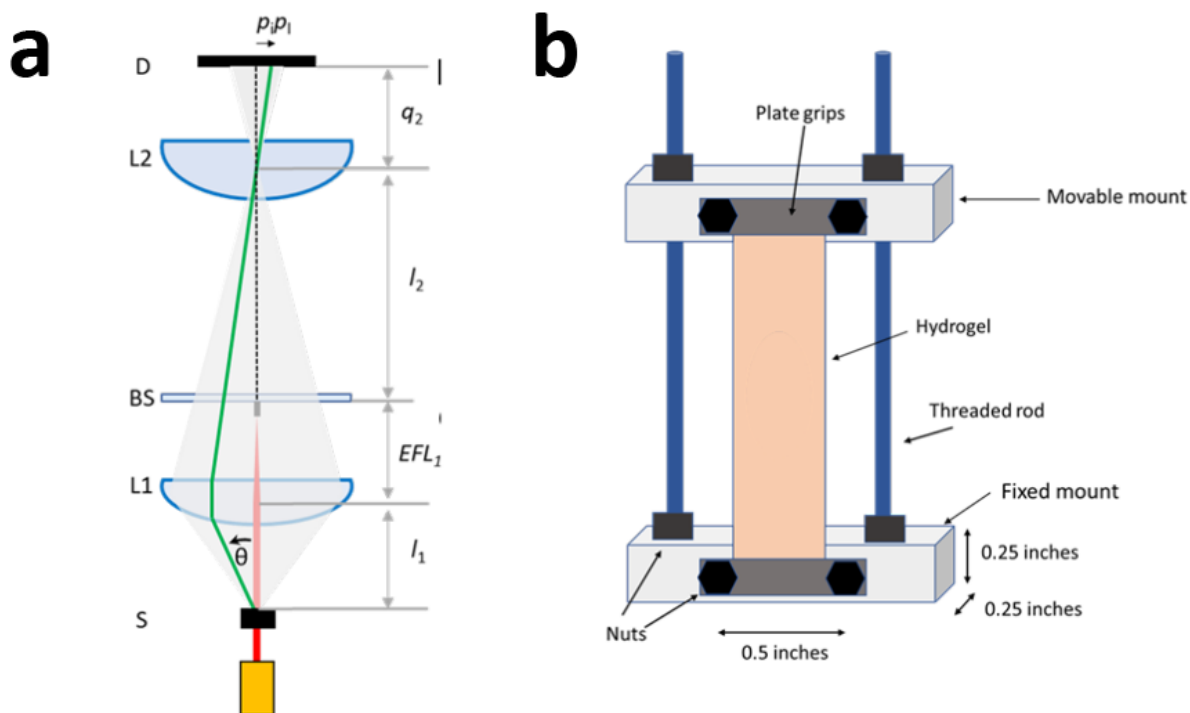


**Figure S26. SALS experimental setup.** a) Schematic diagram of the scattered light where S is the sample,  $\theta$  is the scattering angle, focused by lens L1 through beamstop (BS) through lens L2 to a CMOS detector. b) Scheme of the stretching sample holder.

**Figure S26a** represents the small-angle light scattering (SALS) setup, which has been published previously.<sup>23</sup> The ray diagram shows the initial laser of 625 nm scattered from the sample at an angle  $\theta$  through a convex lens L1 (Edmund Optics-NT67-245) with a numerical aperture, N.A. = 0.85 that captures up to  $58^\circ$  scattered light. The converging scattered light then passes through beam stop and is refocused through another convex lens L2 (Thorlabs-LA 1951A). The beam

stop is at a focal length away from lens L1 and blocks all direct light from the laser. The  $l_1$  and  $l_2$  can be changed to optimize the  $q$ -range. The scattered light is then projected onto a CMOS detector, D (Basler acA800-510 um) which is a focal length away from L2.

A control image is taken using a diffraction grating with 100 lines per mm. This was later used to determine the pixel-to- $q$  conversion for the scattering patterns. The hydrogel was then loaded to the sample setup. The  $l_1$  was set to  $\sim 25$  mm and  $l_2$  to  $\sim 75$  mm. The room lights were then turned off to avoid any background scattering. A scattering image was then taken for each sample.

**Figure S26b** shows a schematic diagram of the sample setup. The hydrogel is held in the setup using plate grips. These plate grips are 0.5 in wide, offering enough space to load the hydrogel. The nuts can be moved allowing the top mount (movable) to move in z-direction. The hydrogel can then be stretched to different lengths.

b. Results

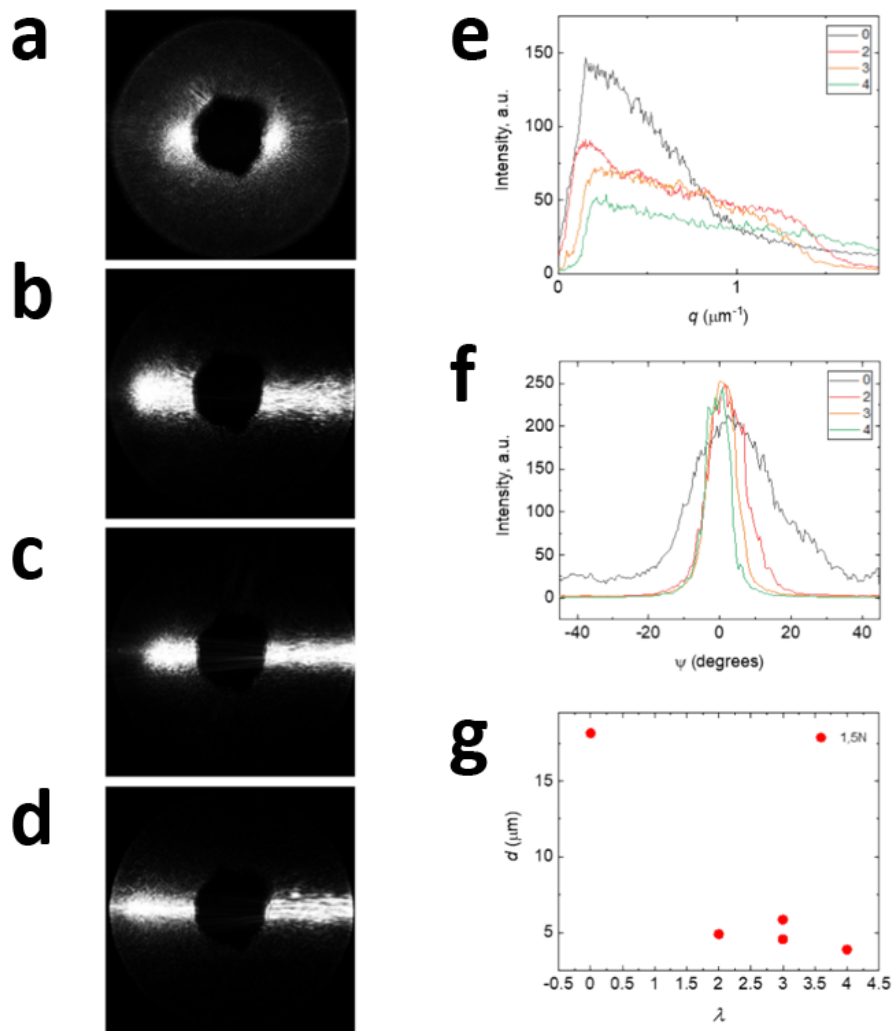


**Figure S27. SALS data for a hydrogel prepared from a 12.5 wt% polymer solution in THF.** 2D scattering plot for a) unstretched and stretched samples at elongation ratios of b) 2, c) 3, and d) 4. e) Intensity versus  $q$  plot at elongation ratios of 0, 2, 3, and 4. f) Intensity versus azimuthal angle,  $\Psi$ , plot at elongation ratios of 0, 2, 3, and 4. g) Pore domain spacing,  $d$ , .

The hydrogel pore domain spacing,  $d$ , and alignment were determined from the 2D scattering plots shown in **Figures S27a – d**. The domain spacing for the unstretched sample was calculated to be  $\sim 20 \mu\text{m}$  in size using the equation,  $d = 2\pi/q^*$ , where  $q^*$  is the primary scattering peak from **Figure S27e**. The asymmetric 2D scattering plots indicate that the hydrogel pores are oriented along the long axis of the gels. As the sample is stretched, the scattering band widens perpendicular to the direction of stretch and decreases in intensity. Simultaneously, the orientation of the pore domains, which is along the fiber, increases, as seen from the narrowing of the scattering band and in the intensity versus azimuthal angle,  $\Psi$ , plot in **Figure S27f**. Furthermore, as the hydrogel is stretched, the in-plane distance between pores decreases from  $\sim 20 \mu\text{m}$  to 2-2.5  $\mu\text{m}$  (**Figure S27g**).

## 18. Property Comparison with Hydrogels in the Literature

**Table S3:** Reported values from the literature for maximum tensile strength, Young’s Modulus, and elongation ratio at break for physical, single network, interpenetrating network, supramolecular, and porous gels. Values not reported are indicated by “NR,” and values with an asterisk were tested under compression. Reported values plotted with permission in Figure 5f of the manuscript.

Hydrogel Class	$\sigma_{\max}$ (MPa)	E (MPa)	$\lambda_b$	Reference in Manuscript
Physical Gel	1.5-5	0.2-5	2.2-3.5	36
Physical Gel	1-7.5	5	4.5-5.0	38
Physical Gel	0.004-0.43	NR	1.4	22
Physical Gel	20-200	NR	8.0	37
Single Network	2.5-5	2-20	3.5-5	12
Single Network	0.4-4	0.01-0.04	2.0-1.9	11
Single Network	0.025-0.4	0.001-2	2.0-8.0	13
Single Network	0.035-0.7	0.0184-0.072	5.0-8.0	4
Single Network	1-9	0.114-10	2.0	14
Interpenetrating Network Gel	50-250	0.008-0.374	1.25-5.0	46
Interpenetrating Network Gel	2.1-3.1	0.5-6.5	4.0-9.0	47
Interpenetrating Network Gel	0.1-17.2	NR	7.0	48

Hydrogel Class	$\sigma_{\max}$ (MPa)	E (MPa)	$\lambda_b$	Reference in Manuscript
Supramolecular	0.5-6	NR	11-15	44
Supramolecular	0.01-0.052	NR	15-33	39
Supramolecular	0.75-2.5	NR	11-21	45
Porous	0.014-0.21*	NR	1.25-1.63*	43
Porous	0.005-0.014*	NR	1.15*	17
Porous	0.025-0.15*	0.96-5.8	1.6*	40
Porous	0.12*	0.0073	1.95*	41
Porous	0.0025-0.015*	0.0015-0.023	1.5*	42

## 15. References

1. Lang C, LaNasa JA, Utomo N, Xu Y, Nelson MJ, Song W, *et al.* Solvent-non-solvent rapid-injection for preparing nanostructured materials from micelles to hydrogels. *Nat Commun* 2019, **10**: 3855.
2. Hillmyer MA, Bates FS. Synthesis and Characterization of Model Polyalkane–Poly(ethylene oxide) Block Copolymers. *Macromolecules* 1996, **29**(22): 6994-7002.
3. Merrill BA. Potassium Naphthalenide. *Encyclopedia of Reagents for Organic Synthesis*. John Wiley & Sons, 2001.
4. Guo C, Bailey TS. Highly distensible nanostructured elastic hydrogels from AB diblock and ABA triblock copolymer melt blends. *Soft Matter* 2010, **6**(19): 4807-4818.
5. Ilavskya J, Jemiana PR. Irena: tool suite for modeling and analysis of small-angle scattering. *J Appl Crystallogr* 2009, **42**: 347-353.
6. Leibler L. Theory of Microphase Separation in Block Copolymers. *Macromolecules* 1980, **13**(6): 1602-1617.
7. Uneyama T, Doi M. Density Functional Theory for Block Copolymer Melts and Blends. *Macromolecules* 2005, **38**(1): 196-205.
8. Werner A, Fredrickson GH. Architectural effects on the stability limits of ABC block copolymers. *J Polym Sci, Part B: Polym Phys* 1997, **35**(5): 849-864.
9. Fredrickson GH. *The Equilibrium Theory of Inhomogeneous Polymers*. Oxford University Press: New York, 2006.
10. Qin J, Grzywacz P, Morse DC. Renormalized one-loop theory of correlations in disordered diblock copolymers. *J Chem Phys* 2011, **135**(8): 084902.
11. Harris CR, Millman KJ, van der Walt SJ, Gommers R, Virtanen P, Cournapeau D, *et al.* Array programming with NumPy. *Nature* 2020, **585**(7825): 357-362.

12. Virtanen P, Gommers R, Oliphant TE, Haberland M, Reddy T, Cournapeau D, *et al.* SciPy 1.0: fundamental algorithms for scientific computing in Python. *Nature Methods* 2020, **17**(3): 261-272.
13. Hansen CM. *Hansen Solubility Parameters: A User's Handbook*, 2nd edn. CRC Press: Boca Raton, FL, 2007.
14. Lodge TP, Hiemenz PC. *Polymer Chemistry*, 3rd edn. CRC Press: Boca Raton, FL, 2020.
15. Frielinghaus H, Hermsdorf N, Almdal K, Mortensen K, Messé L, Corvazier L, *et al.* Micro- vs. macro-phase separation in binary blends of poly(styrene)-poly(isoprene) and poly(isoprene)-poly(ethylene oxide) diblock copolymers. *Europhys Lett* 2001, **53**(5): 680.
16. Özdemir C, Güner A. Solubility profiles of poly(ethylene glycol)/solvent systems, I: Qualitative comparison of solubility parameter approaches. *Eur Polym J* 2007, **43**(7): 3068-3093.
17. Avaz S, Oguz O, Kurt H, Menciloglu YZ, Atilgan C. Soft segment length controls morphology of poly(ethylene oxide) based segmented poly(urethane-urea) copolymers in a binary solvent. *Computational Materials Science* 2017, **138**: 58-69.
18. Dormidontova EE. Role of Competitive PEO–Water and Water–Water Hydrogen Bonding in Aqueous Solution PEO Behavior. *Macromolecules* 2002, **35**(3): 987-1001.
19. Aryanti PTP, Ariono D, Hakim AN, Wenten IG. Flory-Huggins Based Model to Determine Thermodynamic Property of Polymeric Membrane Solution. *Journal of Physics: Conference Series* 2018, **1090**(1): 012074.
20. Deen WM. *Analysis of Transport Phenomena*, 2nd edn. Oxford University Press: New York, 2011.
21. Alhasan R, Tree DR. Gibbs–Duhem Relation for Phase-Field Models of Polymeric Mixtures. *Macromolecules* 2022, **55**(3): 759-765.

22. Tree DR, Delaney KT, Ceniceros HD, Iwama T, Fredrickson GH. A multi-fluid model for microstructure formation in polymer membranes. *Soft Matter* 2017, **13**(16): 3013-3030.
23. Dhakal S, Chen Z, Estrin D, Morozova S. Spatially-Resolved Network Dynamics of Poly(vinyl alcohol) Gels Measured with Dynamic Small Angle Light Scattering. *Gels* 2022, **8**(7): 394.